

This discussion paper is/has been under review for the journal Atmospheric Measurement Techniques (AMT). Please refer to the corresponding final paper in AMT if available.

Microphysical particle properties derived from inversion algorithms developed in the framework of EARLINET

D. Müller¹, C. Böckmann², A. Kolgotin³, L. Schneidenbach^a, E. Chemyakin⁴, J. Rosemann², P. Znak⁵, and A. Romanov⁶

¹School of Physics, Astronomy and Mathematics, University of Hertfordshire, Hatfield, Hertfordshire, UK

²Institute of Mathematics, University of Potsdam, Am Neuen Palais 10, 14469 Potsdam, Germany

³Physics Instrumentation Center, Troitsk, Russia

⁴Science Systems and Applications, Inc., NASA Langley Research Center, Hampton VA, USA

⁵V. A. Fock Institute of Physics, St. Petersburg University, Ulyanovskaya 1, 198504 St. Petersburg, Russia

⁶The National University of Science and Technology, Moscow, Russia

^aformerly at: Institute for Computer Science, University of Potsdam, Am Neuen Palais 10, 14469 Potsdam, Germany

AMTD

8, 12823–12885, 2015

EARLINET inversion algorithms

D. Müller et al.

[Title Page](#)

[Abstract](#)

[Introduction](#)

[Conclusions](#)

[References](#)

[Tables](#)

[Figures](#)

[◀](#)

[▶](#)

[Back](#)

[Close](#)

[Full Screen / Esc](#)

[Printer-friendly Version](#)

[Interactive Discussion](#)



Received: 24 August 2015 – Accepted: 6 October 2015 – Published: 8 December 2015

Correspondence to: D. Müller (d.mueller@herts.ac.uk)

Published by Copernicus Publications on behalf of the European Geosciences Union.

AMTD

8, 12823–12885, 2015

EARLINET inversion algorithms

D. Müller et al.

[Title Page](#)

[Abstract](#)

[Introduction](#)

[Conclusions](#)

[References](#)

[Tables](#)

[Figures](#)

[◀](#)

[▶](#)

[◀](#)

[▶](#)

[Back](#)

[Close](#)

[Full Screen / Esc](#)

[Printer-friendly Version](#)

[Interactive Discussion](#)



Abstract

We present a summary on the current status of two inversion algorithms that are used in EARLINET for the inversion of data collected with EARLINET multiwavelength Raman lidars. These instruments measure backscatter coefficients at 355, 532, and 1064 nm, and extinction coefficients at 355 and 532 nm. Development of these two algorithms started in 2000 when EARLINET was founded. The algorithms are based on manually controlled inversion of optical data which allows for detailed sensitivity studies and thus provides us with comparably high quality of the derived data products. The algorithms allow us to derive particle effective radius, and volume and surface-area concentration with comparably high confidence. The retrieval of the real and imaginary parts of the complex refractive index still is a challenge in view of the accuracy required for these parameters in climate change studies in which light-absorption needs to be known with high accuracy. Single-scattering albedo can be computed from the retrieved microphysical parameters and allows us to categorize aerosols into high and low absorbing aerosols. We discuss the current status of these manually operated algorithms, the potentially achievable accuracy of data products, and the goals for future work on the basis of a few exemplary simulations with synthetic optical data.

The optical data used in our study cover a range of Ångström exponents and extinction-to-backscatter (lidar) ratios that are found from lidar measurements of various aerosol types. We also tested aerosol scenarios that are considered highly unlikely, e.g., the lidar ratios fall outside the commonly accepted range of values measured with Raman lidar, even though the underlying microphysical particle properties are not uncommon. The goal of this part of the study is to test robustness of the algorithms toward their ability to identify aerosol types that have not been measured so far, but cannot be ruled out based on our current knowledge of aerosol physics.

We computed the optical data from monomodal logarithmic particle size distributions, i.e., we explicitly excluded the more complicated case of bimodal particle size distributions which is a topic of ongoing research work. Another constraint is that we

Title Page

Abstract

Introduction

Conclusions

References

Tables

Figures

◀

▶

Back

Close

Full Screen / Esc

Printer-friendly Version

Interactive Discussion



Title Page	
Abstract	Introduction
Conclusions	References
Tables	Figures
	
	
Full Screen / Esc	
Printer-friendly Version	
Interactive Discussion	



only considered particles of spherical shape in our simulations. We considered particle radii as large as 7–10 µm in our simulations. That particle size does not only cover the size range of particles in the fine-mode fraction of naturally occurring particle size distributions but also covers a considerable part of the coarse-mode fraction of particle size distributions. We considered optical-data errors of 15 % in the simulation studies. We target 50 % uncertainty as a reasonable threshold for our data products, though we attempt to obtain data products with less uncertainty in future work.

1 Introduction

The start of EARLINET (European Aerosol Research Lidar Network) in 2000 marked the beginning of the development of inversion algorithms that can be used for the retrieval of aerosol microphysical properties from Raman lidar observations. Based on exploratory work (Qing et al., 1989) it seemed feasible that Raman lidar measurements of backscatter coefficients and extinction coefficients could provide variables such as particle effective radius and complex refractive index from which, under favorable measurement conditions, single-scattering albedo could be derived.

We followed two conceptual approaches. One methodology was developed at the Leibniz Institute for Tropospheric Research (TROPOS), Leipzig, Germany. The development of the methodology continues at the University of Hertfordshire (UH). The second method was developed at the University of Potsdam (UP) (Potsdam, Germany). Both methods in part follow the same basic mathematical concepts in the sense that they are true inversion algorithms. The underlying mathematical equations that connect the microphysical particle properties (which are the variables we are interested in) and the optical properties (which are the variables that are measured with lidar) are solved explicitly. That means we do not carry out forward computations, which commonly are referred to as Mie-scattering computations. We do not use traditional look-up tables that contain an array of microphysical aerosol properties and the optical properties that belong to these microphysical properties. Our approach neglects constraints that

are used in forward computations, as for example the need to prescribe the shape of the particle size distribution as input. The advantage is that we can identify the share of fine-mode and coarse mode particles in particle size distributions, as the inversion algorithms allow us to find approximate solutions of the underlying particle size distributions. The disadvantage is that measurement errors have a direct impact on the quality of the retrieval results. If measurement errors become too large, the inversion algorithms will not be able to find reasonable solutions. The inversion algorithms also respond strongly to systematic errors of the optical input data. This means if calibrations of the optical profiles are not done carefully, or if optical data are faulty because of the incomplete overlap between laser beam and field-of-view of the receiver telescope (Wandinger and Ansmann, 2002), the inversion algorithms will deliver wrong microphysical particle properties.

1.1 Work at TROPOS/UH

With regard to work at TROPOS/UH exploratory algorithm development was based on data we obtained from the first truly operational multiwavelength Raman lidar (Althauser et al., 2000) in the 1990s. This instrument provides backscatter coefficients measured at 355, 400, 532, 710, 800, and 1064 nm and extinction coefficients at 355 and 532 nm. The system uses 4 lasers that operate simultaneously. The high costs of this system and the labor-intensive measurement and data-analysis work showed us fairly early that a wider use of the inversion technology in the lidar community would require reducing the optical data needed for data inversion. Based on exploratory work (Müller et al., 2001b; Veselovskii et al., 2002; Böckmann et al., 2005) it seemed feasible that a Raman lidar consisting of only one Nd:YG laser could still fulfill the minimum requirement with regard to optical data such that successful data inversion could be carried out. This minimum requirement are measurements of backscatter coefficients at 355, 532, and 1064 nm and extinction coefficients at 355 and 532 nm.

The algorithm that was initially developed at TROPOS is based on the concept of Tikhonov's inversion with regularization (Tikhonov and Arsenin, 1977). The algorithm

Title Page	
Abstract	Introduction
Conclusions	References
Tables	Figures
	
	
Back	Close
Full Screen / Esc	
Printer-friendly Version	
Interactive Discussion	



is based on a data-operator controlled environment. That makes this algorithm highly labor-intensive and the output with regard to inversion results is rather low. However, this approach allows us to carry out detailed sensitivity studies in order to test the quality of the data inversion products and to push the envelope in what can theoretically be achieved in terms of aerosol characterization with state-of-the-art multiwavelength Raman lidar. Several sensitivity studies dealt with the ability of the algorithm to retrieve effective radius, and surface-area and volume concentration, and the complex refractive index (CRI) (Müller et al., 1999a, b, 2001b; Veselovskii et al., 2002, 2004). Most sensitivity studies dealt with monomodal particle size distributions, although some work has also been done in the context of bimodal particle size distributions (Veselovskii et al., 2004).

The retrieval of the CRI remains a major challenge in our work. The accuracy requirements for the imaginary part of the CRI are considerable if we want to obtain useful values (high accuracy and precision) of the single-scattering albedo (SSA) which is one of the key parameters in climate change studies. Nowadays we manage to obtain meaningful values of SSA, however at the expense of time-intensive, data-operator-controlled data analysis which involves a careful evaluation of the inversion results (particularly of the CRI). We learnt to retrieve the imaginary part to its correct order of magnitude if it is less than $0.01i$. This value describes moderately light-absorbing aerosol. We learnt to keep the uncertainty bars to approximately $\pm 50\%$ if the imaginary part is larger than $0.01i$. Such values describe strongly light-absorbing particles. We noticed that systematic biases of the imaginary part may occur if its value is close to 0. This bias is naturally introduced as the imaginary part has a minimum value of 0. This lower limit leads to an underestimation of SSA.

We analyzed plenty of different aerosol types in the course of 10 years of measurements, though a statistical significant set of results for each aerosol type still has not been achieved because of the labor-intensive manual data analysis. Examples of aerosol types we analyzed involve urban/industrial pollution over Europe, e.g., Müller et al. (2005), East Asia, e.g., Noh et al. (2011), and South Asia, e.g., Müller et al.

EARLINET inversion algorithms

D. Müller et al.

[Title Page](#)

[Abstract](#)

[Introduction](#)

[Conclusions](#)

[References](#)

[Tables](#)

[Figures](#)

[◀](#)

[▶](#)

[Back](#)

[Close](#)

[Full Screen / Esc](#)

[Printer-friendly Version](#)

[Interactive Discussion](#)



(2001a). We investigated properties of fresh and aged biomass burning aerosols produced in North America, e.g., Müller et al. (2005), Europe, e.g., Alados-Arboledas et al. (2011), and West Africa, e.g., Tesche et al. (2011). We remain cautious with regard to the inversion of optical data that describe non-spherical (mineral dust) particles as to date we do not have a reliable light-scattering model that allows us to describe light-scattering at 180°. We carried out some limited studies in which we used the AERONET light-scattering model as a test on how far we can use this model as it has not been designed for describing particle backscatter coefficients. We conclude from our limited set of studies that we may be able to infer particle effective radius of dust particles and the ratio of spherical-to-non-spherical particles (Veselovskii et al., 2010; Müller et al., 2013).

1.2 Work at UP

The Potsdam algorithm that was developed at UP is based on the concept of using truncated singular value decomposition (TSVD) as regularization method, see e.g., Hansen (2010). This method was adapted to work for the retrieval of the particle size distribution function (PSD) and is called hybrid regularization technique (Böckmann, 2001) since it is using a triple of regularization parameters. Several simulation studies demonstrated that the hybrid method is able to invert monomodal and bimodal PSDs (Böckmann, 2001; Böckmann et al., 2005). The minimum requirements are measurements of backscatter coefficients at 355, 532, and 1064 nm and extinction coefficients at 355 and 532 nm. The inversion of an ill-posed problem, such as the retrieval of the PSD, is always a challenging task because very small measurement errors and tiny rounding errors often will be hugely amplified during the solution process unless an appropriate regularization method is used. Even using a regularization method requires a careful determination of the associated regularization parameters. Therefore, in a next stage of our work we decided to use two regularization techniques in parallel for comparison purposes. The second method is an iterative regularization method based on Páde iteration (Kirsche and Böckmann, 2006; Böckmann and Pornsawad, 2008). Here, the

EARLINET inversion algorithms

D. Müller et al.

[Title Page](#)

[Abstract](#)

[Introduction](#)

[Conclusions](#)

[References](#)

[Tables](#)

[Figures](#)

◀

▶

◀

▶

[Back](#)

[Close](#)

[Full Screen / Esc](#)

[Printer-friendly Version](#)

[Interactive Discussion](#)



number of iteration steps serves as the regularization parameter. This method was adapted and tested successfully to invert the PSD (Böckmann and Kirsche, 2006). The approximated PSD is a linear combination of B splines with appropriately determined weights. The B splines of order d are polynomials of degree $d - 1$. Since the distribution of the B spline nodes also plays a critical role, we endowed the first algorithm TSVD with the possibility to also use non-equidistant node grids (Böckmann, 2001). The iterative method was equipped with an adaptive non-equidistant node grid in (Osterloh et al., 2011).

There is another challenge that needs to be considered. The CRI is actually unknown, too. In order to solve this problem, a grid of viable options for the CRI (all combinations of real parts of CRI (RPCRI) and imaginary parts of CRI (IPCRI)) is assumed, otherwise one additionally has to deal with a non-linear problem. The CRI grid technique is very time consuming, i.e., the computer run time of the inversion process is very large. Therefore, we successfully developed a semi-automated software for spherical particles which is able to run on a parallel processor machine (Osterloh et al., 2009), see Fig. 1. The software is adapted with a tool reading NetCDF-files from the EARLINET data base (The EARLINET publishing group, 2014).

From a mathematical point of view, it is also very important (as a selection criteria for an appropriate regularization method) to investigate the degree of ill-posedness of the problem. Investigations show a moderate ill-posedness (Böckmann et al., 2005; Osterloh et al., 2013) which is not the worst case. Furthermore, first investigations towards non-spherical particles were made. Simulation studies show that the particle shape is an important factor (Böckmann and Wauer, 2001a, b). First retrievals with a two-dimensional spheroidal model, i.e., looking for two-dimensional PSDs depending on radius and aspect ratio, using two-dimensional B splines, can be found in Böckmann and Osterloh (2014). Numerical simulations reveal that the Páde type regularization method is able to retrieve two-dimensional PSDs using backscatter and extinction coefficient profiles, as well as depolarization information.

Title Page	
Abstract	Introduction
Conclusions	References
Tables	Figures
	
	
Full Screen / Esc	
Printer-friendly Version	
Interactive Discussion	



The semi-automatic software was applied to measurement cases. We analyzed Raman lidar measurement data with three backscatter coefficients at 355, 532, and 1064 nm and two extinction coefficients at 355 and 532 nm. From those optical particle variables we retrieved microphysical particle properties of different aerosol types. Successful retrievals have been made for biomass-burning and industrial-pollution aerosols over Germany (Wandinger et al., 2002), continental aerosols (Eixmann et al., 2002), Arctic haze aerosols (Hoffmann et al., 2012), biomass-burning aerosols over Romania (Osterloh et al., 2013) and over Athens (Papayannis et al., 2008). Moreover, the two-dimensional spheroidal model was applied to a measurement scenario of Saharan dust observed over Barbados (13.16° N, 59.44° W). We found promising results, in particular, when we used additional depolarization profiles (Böckmann et al., 2012). Finally, in Samaras et al. (2015) a direct quantitative comparison of the retrieved microphysical properties with measurements from a Compact Time of Flight Aerosol Mass Spectrometer (AMS) was used to validate the algorithm for spherical particles. Focusing on the fine mode we observed remarkable similarities between the retrieved PSD and the one measured by the AMS. Additionally, microphysical retrievals performed with sun photometer data were also used to explore the results for biomass burning aerosols.

Section 2 summarizes the two methodologies. Section 3 presents some simulation studies that illustrate the current status. Section 4 closes with a summary and outlook.

2 Methodology

The microphysical properties are derived from solving Fredholm integral equations of the first kind (Müller et al., 1999a; Veselovskii et al., 2002; Böckmann, 2001; Böckmann et al., 2005; Ansmann and Müller, 2005). These equations can be written in general terms as

$$g_i^*(\lambda_i) = \int_0^\infty K_i(m, r, \lambda_i, s) f^*(r) dr, \quad (1)$$

EARLINET inversion algorithms

D. Müller et al.

Title Page

Abstract

Introduction

Conclusions

References

Tables

Figures

|◀

▶|

◀

▶

Back

Close

Full Screen / Esc

Printer-friendly Version

Interactive Discussion



EARLINET inversion algorithms

D. Müller et al.

[Title Page](#)[Abstract](#)[Introduction](#)[Conclusions](#)[References](#)[Tables](#)[Figures](#)[|◀](#)[▶|](#)[◀](#)[▶](#)[Back](#)[Close](#)[Full Screen / Esc](#)[Printer-friendly Version](#)[Interactive Discussion](#)

The term $g_p^*(\lambda_i)$ denotes the exact optical data at the measurement wavelength λ_i . The optical data usually have an uncertainty as we use experimental data. The subscript p denotes the type of optical data, i.e., β denotes particle backscatter coefficients and α denotes particle extinction coefficients.

The backscatter and extinction kernel functions are denoted by $K_\beta(m, r, \lambda, s)$ and $K_\alpha(m, r, \lambda, s)$. The kernel functions depend on the complex refractive index m of the particles, i.e., $m = m_R - m_I i$. The term m_R denotes the real part. The term $m_I i$ denotes the imaginary part of the CRI. The radius of the particles is denoted as r . The shape properties s of the particles determine their backscatter and extinction properties. We only consider spherical shape of the particles and therefore drop this parameter in the following discussion.

The kernel functions $K_p(m, r, \lambda_i)$ are calculated from Mie-scattering theory (Bohren and Huffman, 1983). The term $f^*(r)$ describes the exact (true) particle size distribution which is described as the number of particles per unit volume between particle radius r and $r + dr$.

Equation (1) can be written as

$$g_p^* = \int_{r_{\min}}^{r_{\max}} K_p(m, r) f^*(r) dr + \epsilon_p^{\text{limits}}. \quad (2)$$

The term g_p^* describes the exact values of the optical data. The subscript $p = (\beta, \lambda_i)$ describes the kind of the optical input data at given wavelength. The lower and upper integration limit of the particle radii within which the inversion is performed are denoted by r_{\min} and r_{\max} . We write this radius interval as $[r_{\min}, r_{\max}]$. The term $\epsilon_p^{\text{limits}}$ represents the model error that results from the fact that the integration limits are not from 0 to ∞ .

Disregarding the model error term we obtain

$$g_p^* = \int_{r_{\min}}^{r_{\max}} K_p(m, r) f_M(r) dr. \quad (3)$$

[Title Page](#)[Abstract](#)[Introduction](#)[Conclusions](#)[References](#)[Tables](#)[Figures](#)[|◀](#)[▶|](#)[Back](#)[Close](#)[Full Screen / Esc](#)[Printer-friendly Version](#)[Interactive Discussion](#)

The investigated PSD $f_M(r)$ is obtained from the numerical solution of Eq. (3) (Twomey, 1965; Zuev and Naats, 1983; Engl et al., 1996; Hansen, 2010). The numerical solution is not an easy task since this compact Fredholm operator is ill-posed. Firstly, the expression $f_M(r)$ is approximated by a sum that consists of the linear superposition of base functions

$$f_M(r) = f(r) + \epsilon(r) = \sum_{j=1}^{N_B} f_j B_j(r) + \epsilon(r). \quad (4)$$

The term $f(r)$ is an approximation of the solution of Eq. (3). The expression f_j describes weight coefficients. $B_j(r)$ are B-spline base functions. N_B is the number of used base functions. The term $\epsilon(r)$ is the discretization error. This error is caused by discretizing the PSD with the linear combination of base functions.

Neglecting the discretization error term we can write the optical data as linear combination by using Eqs. (3) and (4), i.e.,

$$g_p = \sum_{j=1}^{N_B} A_{pj}(m) f_j. \quad (5)$$

The matrix elements A_{pj} are calculated from the kernel functions and the base functions as

$$A_{pj} = \int_{r_{\min}}^{r_{\max}} K_p(m, r) B_j(r) dr. \quad (6)$$

If we write the optical data as vector $\mathbf{g} = [g_p]$ and the weight coefficients as vector $\mathbf{f} = [f_j]$ we can write Eq. (5) as a vector–matrix expression, i.e.,

$$\mathbf{g} = \mathbf{A}\mathbf{f}. \quad (7)$$

The matrix $\mathbf{A} = [A_{pj}]$ is rectangular. It is called weight matrix. The elements of this matrix are calculated from Eq. (6).

Since the operator is ill-posed as mentioned above the resulting linear equation system Eq. (7) is ill-conditioned. Therefore, the system cannot be solved by standard routines. One needs particular regularization techniques to solve such systems.

The unknown vector of the weight coefficients \mathbf{f} is connected by the matrix operator \mathbf{A} with the optical data vector \mathbf{g} . Notice, the data vector \mathbf{g} contains measurement errors. For ill-conditioned systems this means that small data errors may be amplified strongly during a standard solution process. Finally, the total error contains the measurement error and the mathematical approximation errors in an additive way.

The TROPOS/UH algorithm and the UP algorithm use different appropriate regularization methods. The first one uses Tikhonov regularization (Phillips, 1962; Tikhonov and Arsenin, 1977) and the latter one deals with regularizing truncated singular value decomposition (TSVD) (Engl et al., 1996; Hansen, 2010). Details of both algorithms are described in the next subsections.

2.1 TROPOS/UH algorithm

2.2 Solving the Fredholm equations

Detailed descriptions of solving the modified version of Tikhonov's inversion algorithm the way it is used in our work is explained in detail by Müller et al. (1999a) and Veselovskii et al. (2002).

The number of base functions, N_B is equal or exceeds the number of optical data. Veselovskii et al. (2002, 2004) prefer to keep the number of base functions nearly equal to the number of input optical data.

In the case of the algorithm developed at TROPOS the base functions have triangular shape on a logarithmic radius scale (Müller et al., 1999a, b). We tested two other shapes of base functions, i.e., histogram columns (Heintzenberg et al., 1981) and monomodal logarithmic-normal distributions (Amato et al., 1995). We did not find

Title Page

Abstract

Introduction

Conclusions

References

Tables

Figures

|◀

▶|

◀

▶

Back

Close

Full Screen / Esc

Printer-friendly Version

Interactive Discussion



significant improvement of our data products if we use these shapes of base functions. We believe that one main cause for this result is the fact that the main error sources in data inversion are incorrect optical input data g_p , unknown complex refractive index and uncertainties caused by the regularization procedure. All these errors outweigh

5 the potential improvements that could be obtained by using a more suitable description of the investigated PSDs, e.g., base functions of logarithmic-normal shape. The base functions of second order, i.e., first degree that we use have also shown to work sufficiently well for the reconstruction of PSDs of bimodal shape (Veselovskii et al., 2004).

10 We can solve Eq. (7) by introducing the transposed matrix \mathbf{A}^T . Assuming the existence we use $(\mathbf{A}^T \mathbf{A})^{-1}$ as the inverse of matrix $\mathbf{A}^T \mathbf{A}$. In that way we obtain the simple normal solution of Eq. (7) for the weight factors, i.e.,

$$\mathbf{f} = (\mathbf{A}^T \mathbf{A})^{-1} \mathbf{A}^T \mathbf{g}. \quad (8)$$

15 The solution of Eq. (8) usually leads to physically useless results because the mathematical problem is ill-posed. The reason for it is that the matrix-operator \mathbf{A} is ill-conditioned since it is the discretized representative of an infinite dimensional ill-posed operator. Details on this property can be found in, e.g., Twomey (1977). Explanations can also be found in, e.g., Müller et al. (1999a) who provide details on how to overcome this problem. Briefly, we introduce the equation (Twomey, 1977; Tikhonov and Arsenin, 20 1977)

$$(\mathbf{A}^T \mathbf{A} + \gamma \mathbf{H}) \mathbf{f} = \mathbf{A}^T \mathbf{g}. \quad (9)$$

25 The expression \mathbf{H} is the smoothing matrix operator (Twomey, 1977). This operator describes the physical constraint that the retrieved PSD does not show “large” oscillations in the size range for which the PSD is retrieved. This size range is determined by the inversion window.

Title Page

Abstract

Introduction

Conclusions

References

Tables

Figures

◀

▶

◀

▶

Back

Close

Full Screen / Esc

Printer-friendly Version

Interactive Discussion



Details on the appropriate choice of \mathbf{H} can be found in Twomey (1977). \mathbf{H} influences the maximum difference between the weight factors of successive base functions. γ is the Lagrange multiplier. It is the non-negative regularization parameter that determines the degree of smoothing of the investigated PSDs, i.e., the strength of the operator \mathbf{H} .

5 2.2.1 Identification of the solution space

The solution finding requires the application of several constraints. These constraints stabilize the inversion problem and help us reject mathematical solutions that are physically not reasonable. We use the simplifying assumption of a wavelength- and size-independent complex refractive index of the aerosol particles.

10 The rationale for using a gliding inversion window is given by Müller et al. (1999a, b). We used to apply 50 inversion windows (Müller et al., 1999a) but subsequently moved to 400 windows. We find that the quality of the retrieval can be improved if we use more inversion windows on a smaller radius search grid. Figure 1 in Müller et al. (1999a) shows how the inversion windows are formed.

15 We also discretize the CRI search space. In this contribution the real part m_R varied from 1.325 to 1.8 with step 0.025. The imaginary part, $i \cdot m_I$, varies from 0 to $i \cdot 0.05$ with step $i \cdot 0.003$.

In that way we obtain k individual mathematical solutions for a given optical data set. Each solution number k is characterized by an inversion window $[r_{\min}^{(k)}, r_{\max}^{(k)}]$ and a CRI value $m^{(k)} = m_R^{(k)} - i \cdot m_I^{(k)}$, which defines the vector $\mathbf{f}^{(k)}$ of the weight coefficients and the vector $\mathbf{g}^{(k)}$ of the optical data that can be backcalculated from the inversion results, i.e.,

$$20 \quad \mathbf{A}^{(k)} \mathbf{f}^{(k)} = \mathbf{g}^{(k)}. \quad (10)$$

We calculate the discrepancy vector, as introduced by Veselovskii et al. (2002),

$$25 \quad \rho^{(k)} = \mathbf{A}^{(k)} \left| \mathbf{f}^{(k)} \right| - \mathbf{g} \quad (11)$$

Title Page

Abstract

Introduction

Conclusions

References

Tables

Figures

◀

▶

◀

▶

Back

Close

Full Screen / Esc

Printer-friendly Version

Interactive Discussion



and the normalized discrepancy value

$$\rho^{(k)} = \frac{1}{N_O} \sum_{j=1}^{N_O} \frac{\rho_j^{(k)}}{g_j} 100\%. \quad (12)$$

The symbol $|\cdot|$ means that every element of the vector $f^{(k)}$ is converted into its absolute value. The number of optical data is N_O . The term $\rho_j^{(k)}$ denotes the j th component of vector $\rho^{(k)}$. The j th component of vector g is g_j .

The simulations were carried out with the model data and with uncertainties added to the data. The main purpose of the simulation with erroneous data was to learn by how much the inversion products could deviate from the exact results for various error levels. We tried to answer this question by distorting the optical data such that extreme changes (distortions) of the spectra of the backscatter coefficients (at 355, 532, and 1064 nm) and the spectra of the extinction coefficients (at 355 and 532 nm) could be achieved. We assumed an uncertainty of 5, 10, and 15 % for the data points. For example in the case of 15 % error, each data point in the first step was distorted by up to 15 %, and independently of the other data points of a given 3 backscatter +2 extinction data set. The inversion was carried out for this distorted optical data set. In the next step, the optical data of the original (error free) optical data set were again distorted by up to 15 %, and the inversion was carried out a second time. We repeated this procedure 8 times, and in this way obtained 8 different solutions. We then averaged these 8 solutions which provides us with a mean value of the inversion of the erroneous data set and an uncertainty bar in terms of 1-standard deviation.

2.2.2 Particle size distributions: examples

Table 1 summarizes the parameters of the PSDs that were used in the simulation studies. Additional explanations are given in Sect. 3.1.

[Title Page](#)[Abstract](#)[Introduction](#)[Conclusions](#)[References](#)[Tables](#)[Figures](#)[◀](#)[▶](#)[◀](#)[▶](#)[Back](#)[Close](#)[Full Screen / Esc](#)[Printer-friendly Version](#)[Interactive Discussion](#)

Figure 2 shows examples of retrieved PSDs with the TROPOS/UH algorithm. The task of deriving the shape of the particle size distribution is challenging as we are dealing with a small number of optical data, i.e., the information content of the set of optical data is low. However, during our development work we noticed that we can obtain some information on the particle size distribution, too.

The panel shows the results for moderately absorbing aerosols, i.e., the imaginary part is $0.01i$. The first row (a–c) shows the results for error free data and the assumption that the real part can be derived to an uncertainty of 0.1. The second row (d–f) shows the results for error free data and the ideal case that we can derive the real part to 0.05 accuracy. The rationale for using these uncertainties of 0.1 and 0.05 will be given in Sect. 3.1. The third row (g–i) shows the results for a measurement error of 15 % and an uncertainty of 0.1 of the real part. The fourth row (j–l) shows the results for the measurement error of 15 % and an uncertainty of 0.05 of the real part.

The left plot of each row (a, d, g, j) shows the results for a mean radius of 60 nm. The middle plot in each row (b, e, h, k) shows the results for a mean radius of 140 nm. The right plot of each row (c, f, i, l) shows the results for 300 nm mean radius. These three mean radii convert to effective radii of 0.23, 0.55, and 1.2 μm . The numbers describe one PSD (in volume-concentration presentation) for which particles are mainly in the fine-mode fraction (left column), one PSD for which particles are in the fine- and coarse-mode fraction (center column), and one PSD for which the particles mainly are in the coarse-mode fraction (right column).

We see that the shape of the particle size distributions can be derived to some degree. The individual solutions in general exhibit the same features. The panel shows that we may not be able to derive the exact shape of the particle size distributions. The individual PSDs show peaks that are not exactly at the position of the peak of the true PSD. Nevertheless, if we average all individual PSDs the mean solution is comparably close to the true PSD.

EARLINET inversion algorithms

D. Müller et al.

Title Page

Abstract

Introduction

Conclusions

References

Tables

Figures

◀

▶

◀

▶

Back

Close

Full Screen / Esc

Printer-friendly Version

Interactive Discussion



2.3 UP algorithm

2.4 Solving the Fredholm equations and description of the software

The Potsdam algorithm (UP) via TSVD as a hybrid regularization method is using collocation with B splines $B_j(r)$, $j = 1, \dots, n$, of variable order d . The discretization technique of the Fredholm integral Eq. (3) itself follows the same rules as the TROPOS/UH algorithm, see Eqs. (6) and (7). For more details about the TSVD see also Engl et al. (1996), Hansen (2010), and Böckmann (2001). In contrast to the TROPOS/UH algorithm the UP method is using the number n and the order d of the B splines as the first two regularization parameters. The TROPOS/UH algorithm is using fixed order 2, namely B splines with triangular shape. We found in using TSVD that the number and shape of the B splines has a large influence on the accuracy of the inverted PSD. Our experience shows that $n = 3, \dots, 8$ and $d = 3, 4$ are the most appropriate parameters. The discretization dimension (number n of used B splines) has regularization properties, a well-known fact, see e.g., Hansen (2010). The matrix \mathbf{A} is decomposed uniquely into $\mathbf{A} = \mathbf{V}^T \mathbf{D} \mathbf{U}$ with orthonormal matrices \mathbf{U} and \mathbf{V} , and \mathbf{D} is a rectangular diagonal matrix containing the non-negative singular values clustering to zero. Since small singular values are amplifying the data noise (measurement errors) and generate oscillations in the solution, namely the PSD, it is necessary to truncate them. The truncation level of the singular values $k = 0, \dots, \min(5, n) - 1$ is the third regularization parameter of the hybrid method. This results in a triple (d, n, k) of parameters. The linear equation system $\mathbf{Af} = (\mathbf{V}^T \mathbf{D} \mathbf{U})\mathbf{f} = \mathbf{g}$ with matrix \mathbf{A} from Eq. (6) has to be solved for each parameter triple, e.g., $n = 3, \dots, 8$, $d = 3, 4$ and $k = 0, \dots, \min(5, n) - 1$. The PSD $f(r)$ is determined via linear combination with the particular B splines (number and order) as $f(r) = \sum_{j=1}^n f_j B_j(r)$. For details on the additionally included non-negative constraint for the PSD see Böckmann (2001).

The spline number n and order d are not independent parameters; they are related to each other through the number of B spline nodes. The algorithm has the possibility to use an equidistant or a non-equidistant node grid. For the latter we employ

AMTD

8, 12823–12885, 2015

EARLINET inversion algorithms

D. Müller et al.

Title Page

Abstract

Introduction

Conclusions

References

Tables

Figures

◀

▶

◀

▶

Back

Close

Full Screen / Esc

Printer-friendly Version

Interactive Discussion



a non-equidistant grid using the Chebyshev polynomial roots for the nodes that are transformed into the interval $[r_{\min}, r_{\max}]$ to avoid for frequently observed characteristics, e.g., oscillations, of the PSD.

Figure 1 shows a screenshot of the developed software. The workflow of the software is split into a setup-, a computation-, and an evaluation step. The setup step allows the user to specify input data, to define the parameter space to search, to configure a simulation, and to select retrieval methods. The goal of this step is to create a job description that is fed into the computation step.

For the computation step, we have developed a parallel software to cope either with the vast parameter space or to enable a more refined search for a solution. This part of the software is designed to run separately from the interactive setup and evaluation step in order to allow for parallel execution on a supercomputer or a computer cluster. A master process splits the work into small units and delegates the calculation to any available worker process. Once a worker has completed its task, it returns the results to the master. The current search algorithm allows for what we describe as embarrassingly parallel processing (i. e. it does not require any interaction between the workers and therefore scales to a large number of workers, see Osterloh et al., 2009).

The screenshot in Fig. 1 was taken from the result evaluation step after a completed computation. The QT-based front-end allows the user to interactively explore the results and to plot further details (right box) for selected coordinates (grid points) (left box).

It is obvious that, by including the wavelength- and size-independent complex refractive index grid, see Fig. 1 (left box) the solution space of the algorithm is quite huge, consisting of $|n| \times |d| \times |k| \times |\text{IRPCRII} \times \text{IIPCRII}|$ solutions overall, where $|\cdot|$ denotes the amount of different values of the specific parameter. The solution space is restricted in the following way: For every specific refractive index the best triple (d, n, k) is picked in terms of least residual error using forward calculation of Eq. (3) in contrast to the TROPOS/UH algorithm where Eq. (7) is used. Afterwards the best triple at each grid point is used and the associated least residual error is presented with a logarithmical color scale relevant to the error magnitude, see Fig. 1. This visual representation is

EARLINET inversion algorithms

D. Müller et al.

Title Page

Abstract

Introduction

Conclusions

References

Tables

Figures

◀

▶

◀

▶

Back

Close

Full Screen / Esc

Printer-friendly Version

Interactive Discussion



EARLINET inversion algorithms

D. Müller et al.

[Title Page](#)[Abstract](#)[Introduction](#)[Conclusions](#)[References](#)[Tables](#)[Figures](#)[◀](#)[▶](#)[Back](#)[Close](#)[Full Screen / Esc](#)[Printer-friendly Version](#)[Interactive Discussion](#)

not truly noiseless. Even those small errors can be harmful for an ill-posed inversion problem.

For the post-processing procedure we manually select the “best” complex refractive indices depending on the “best” PSDs. In Fig. 3 we show a few examples using noiseless data for fine-mode particles ($\text{gsd } \sigma = 1.5$) with real part of the CRI of 1.5 (left two columns) and for fine-coarse-mode particles ($\text{gsd } \sigma = 2.1$) with real part 1.5 (middle two columns) and again for $\sigma = 2.1$ with real part 1.4 (right two columns). The rows indicate non-absorbing and absorbing particles from top to bottom. The imaginary parts of CRI are $0i$, $0.005i$, $0.01i$ and $0.05i$. In Fig. 3 we show mostly the maximum norm except for (e), (i), (k) and (m) where the 2-norm of the absolute error is screened.

The selection procedure is easier for fine-mode particles, see Fig. 3 first column, than for fine-coarse- and coarse-mode particles (not shown here) since the “best” CRIs are located on a very thin diagonal, in particular, for real part 1.5 as shown in Fig. 3a, g, m, s. We guess that “underneath” the diagonal structure some kind of lack on information is hidden that keeps us from determining the refractive index uniquely. However, we will give an estimation for the CRI using the mean of approximately 10 to 20 “best” values; details are given below.

For the real part 1.4 the diagonal structure disappears more or less for fine-coarse- (see Fig. 3e, k, q) and coarse-mode particles (not shown here) except for strong light-absorbing particles with imaginary part $0.05i$, see Fig. 3w. We observe a similar behavior for the same particle types with real part 1.6 and non- or weakly-absorbing particles (imaginary part $0i$ and $0.005i$), not shown here. All columns of Fig. 3 show that the selection procedure becomes easier with increasing imaginary part. Note that we did not use larger coarse-mode particles, e.g., with $\sigma = 2.5$ in our simulation study because of the ill-posedness from a mathematical point of view, i.e., the smoothness of the kernel function in Eq. (1). Those investigations show that the Potsdam algorithm should not be used for radii larger than $5\text{--}7 \mu\text{m}$ (rule of thumb), see Osterloh et al. (2013), Samaras et al. (2015).

Title Page

Abstract

Introduction

Conclusions

References

Tables

Figures

◀

▶

Back

Close

Full Screen / Esc

Printer-friendly Version

Interactive Discussion



2.4.1 Identification of the solution space

In this section we explain the selection procedure of CRI and PSD. The main selection criteria are based on experiential knowledge for a grid mesh of 30×30 until 60×60 grid points, see Figs. 1 and 3.

5 First, if grid points of the CRI are located on a diagonal they can be collected into one cluster as long as they result in a good representation of the PSD. Isolated grid points which are not located in a cluster inside the diagonal region or in a cluster inside an arbitrarily shaped region should be removed even for the case of a good mathematical approximation of the PSD. But usually the approximation of the PSD resulting from
10 isolated grid points is not very good. Physically meaningful PSDs appear in clusters.

Second, if grid points form a thin vertical or horizontal line and additionally provide a bad approximation of the solution, i.e., of the PSD, all data points along the vertical or horizontal line should be removed. If grid points appear isolated at the end of a diagonal or an arbitrarily shaped region (we denote them as boundary points) they may be
15 removed, for example, if too many grid points are suitable, see next paragraph.

Third, as a rule of thumb one should select at least 10 grid points (if necessary in using accumulative 2 or 3 norm grids (as previously explained)) with a maximum of 20. If more than one cluster exists and if it has the same number of solutions it is difficult to decide which cluster should be preferred. Changing the mathematical measure (norm
20 grid) may help in the decision making. For more details see (Samaras et al., 2015).

Finally, for fine-mode particles ($\sigma = 1.5, 1.7$, i.e., narrow mono-lognormal PSD) we suggest to use an equidistant B-spline node grid whereas our experience shows that better results can be achieved for coarse-mode particles ($\sigma = 2.3$, expanded mono-lognormal PSD) with a non-equidistant grid of left-hand Chebyshev nodes.

25 Furthermore, using the Páde iteration as regularization method leads often to very good results with respect to the “pattern” of the obtained refractive index grid. Therefore, the manually-controlled selection process of the CRI, as described above, is often easier to achieve than using TSVD regularization. This is especially true for the PSD

Title Page	
Abstract	Introduction
Conclusions	References
Tables	Figures
	
	
Full Screen / Esc	
Printer-friendly Version	
Interactive Discussion	



examples with $\sigma = 1.5, 1.7, 1.9$ (fine- and intermediate-mode particles) independently of the real and imaginary part of the CRI. In all cases, the selection process of the CRI grid points associated with the “best PSD solutions” is very easy since the “best solutions” in most CRI grids form distinctive diagonals (not shown here). No isolated grid points occur in general, i.e., all points are located in clusters. In case of absence of a diagonal structure, experience shows that one could locate meaningful solutions in arbitrarily-shaped clusters too, see Samaras et al. (2015). Coarser modes, $\sigma = 2.1, 2.3$, seem to be occasionally problematic in terms of seeking a solution-cluster, which could lead to oscillatory PSDs. This is a huge improvement. Nevertheless, it should be mentioned that the retrieved mean PSD is less accurate for small radii compared to the PSD obtained with TSVD. Therefore, the Páde iteration was not used in this simulation study. It is an ongoing work to combine both methods in an appropriate way to make use of the different advantages associated with both methods.

2.4.2 Particle size distribution: examples

The UP algorithm was tested with the same examples, see Table 1, as the TRO-POS/UH algorithm.

Selecting the best CRI grid points, i.e., the mean CRI, is always strongly connected with the corresponding PSD, i.e., we look for similar shapes of the PSD. The mean retrieved PSD solution, Figs. 3 and 4 (red solid line), is the average of all selected CRI grid points, which in most cases correspond to 10 to 20 PSD's (grey solid lines), see Figs. 3 and 4 (initial PSD: black solid line).

Figure 3 shows 12 examples of retrieved PSDs in the noiseless data case. In that case it is possible to retrieve the mono-lognormal shape of the input PSD very well with regard to accuracy and precision in almost all examples, in particular peak height and location match accurately, see Fig. 3. For the coarse-mode particles (gsd $\sigma = 2.3$, not shown here) a second peak very often occurs, although this second peak is very small in most cases. The exception are weakly absorbing ($0.005i, 0.01i$) particles with real part 1.4. In that case the PSD is monomodal. For non-absorbing particles or strong

Title Page	
Abstract	Introduction
Conclusions	References
Tables	Figures
◀	▶
◀	▶
Back	Close
Full Screen / Esc	
Printer-friendly Version	
Interactive Discussion	



EARLINET inversion algorithms

D. Müller et al.

[Title Page](#)[Abstract](#)[Introduction](#)[Conclusions](#)[References](#)[Tables](#)[Figures](#)[◀](#)[▶](#)[Back](#)[Close](#)[Full Screen / Esc](#)[Printer-friendly Version](#)[Interactive Discussion](#)

light-absorbing particles ($0.05i$) with real part 1.4 the second peak also occurs for gsd $\sigma = 2.1$, see Fig. 3f and x and gsd $\sigma = 1.9$, not shown here.

In summary, only for coarse-mode particles and for almost all real and imaginary parts (not shown here) and for fine-coarse-mode particles with real part 1.4 and imaginary part $0i$ (Fig. 3f) or $0.05i$ (Fig. 3x) the retrieved PSDs show a small second peak, but this is probably only a mathematical feature (oscillation) which cannot be smoothed out during the regularization process, probably because of the larger ill-posedness of the underlying mathematical problem.

Figure 4 shows 24 examples for the retrieved PSDs in the case of noisy data (random Gaussian noise of 15 %, 10 runs per example). Most of the results are good, in particular for gsd 1.7 and 1.9. In the case of noisy input data, oscillations of the PSDs for coarse-mode particles occur and show a second or even a third peak for all CRIs, i.e., gsd $\sigma = 2.3$. Examples are shown in Fig. 4d, f, j, l, p, r, v, x; accuracy is good (except for strong light-absorbing particles with $0.05i$, see Fig. 4v and x) but precision is not. Additionally, all PSDs coupled with real part 1.4 and gsd 1.7–2.1 show more or less a second peak for all imaginary parts (not shown here).

For fine-mode particles with gsd $\sigma = 1.5$ the retrieved PSD is always monomodal. But the peak height is underestimated and the peak is shifted to larger radii (see Fig. 4a, e, g, k, m, q, s, w); the precision is still good but the accuracy is lower. The impact (quantity) of both effects (location and height of the peak) is decreasing with increasing real part, independent of the value of the imaginary part. Examples are shown in Fig. 4, first and fifth column.

For real parts 1.5 and 1.6 in combination with $\sigma = 1.7, 1.9$ the retrieved PSD (red solid lines) is monomodal. The peak height and its location overlap excellently the ones of the initial distribution (black solid lines) for all imaginary parts. Examples are shown in Fig. 4, second and third column. Therefore, here the accuracy and precision is very high even in the case of noisy data. In contrast, for $\sigma = 2.1$ (not shown here) the peak height is often a little bit overestimated, but the peak location undergoes only a small shift to the left or right.

In summary, with 15 % noise added to the input data, the PSD can still be retrieved very well for fine-coarse-mode particles with real parts 1.5 and 1.6 in combination with all imaginary parts.

AMTD

8, 12823–12885, 2015

EARLINET inversion algorithms

D. Müller et al.

Title Page	
Abstract	Introduction
Conclusions	References
Tables	Figures
	
◀	▶
Back	Close
Full Screen / Esc	
Printer-friendly Version	
Interactive Discussion	



3 Simulation results and discussion

5 3.1 Generation of optical data for retrieving microphysical parameters

Table 1 shows the parameters of the particle size distributions (effective radius and geometric standard deviation) and the CRI that were used for the computations of the optical input data. We used 5 different effective radii. Effective radii of 0.15 and 0.2 μm are in the size range of the fine-mode fraction of particle size distributions. Effective
10 radii of 0.28 and 0.4 μm describe particle size distributions that have a significant share of particles in the coarse-mode fraction and the fine-mode fraction. An effective radius of 0.57 μm describes a size distribution for which most of the particles are in the coarse-mode fraction of the particle size distribution.

With regard to the complex refractive indices we tested 3 real parts, i.e., 1.4, 1.5,
15 and 1.6. To our opinion these values cover a realistic range of real parts that can be expected for atmospheric particles. Values of around 1.4 describe highly refractory particles. Sea salt belongs to this class of particles. The value of 1.5 can be used to describe industrial pollutants as for example sulfuric acid. Soot has a high real part of 1.8, but usually it is not found in pure form. Thus, if soot mixes with other aerosol
20 components the real part reduces. We estimate that 1.6 is a representative value of pollution, as for example biomass-burning particles that contain some amount of black carbon.

The imaginary part varies over several orders of magnitude. Our goal is that we can find the correct value at least to within $\pm 50 \%$.

25 An accuracy of approximately ± 0.03 for single-scattering albedo is often assumed as basic requirement in order to test the sensitivity of light-absorbing aerosols in climate

Title Page	
Abstract	Introduction
Conclusions	References
Tables	Figures
	
◀	▶
Back	Close
Full Screen / Esc	
Printer-friendly Version	
Interactive Discussion	



change studies. This accuracy, however, cannot be expressed in terms of a single number of the accuracy of the imaginary part. The reason for it is that the particle size distribution also influences the value of SSA. A small change of the imaginary part may have a large impact on SSA if the particles are in a specific radius range. A small change of the imaginary part may not have a significant impact on SSA if the particles are in another part of the radius range of atmospheric particles. In the first step we tested if we are able to derive the imaginary part to within ± 0.005 in absolute values. This accuracy may not be achievable all the time, but it would significantly increase our chances to retrieve highly accurate values of single-scattering albedo.

We had to restrict our simulations to a few imaginary parts because the inversion algorithms are manually operated and the data analysis is time consuming. We selected a few imaginary parts that were meant to give us a reasonable overview on the retrieval performance if particles are non-absorbing (imaginary part = $0/i$) and if particles are highly light-absorbing (imaginary part = $0.05/i$).

One point that must be considered in these simulations is the fact that we likely will not find all possible combinations of the particle size parameters (effective radius, real and imaginary part of the complex refractive index) listed in Table 1. The reason why we believe that this will not happen can be seen from the following Table 2.

Table 2 shows the minimum and maximum values of the extinction-related and backscatter-related Ångström exponents that follow from the combinations of the 5 effective radii and the CRIs listed in Table 1. The other three values (5 in total) for each of the Ångström exponents falls within these minimum and maximum values. We also show the individual values of the lidar ratios, and the ratio of the two lidar ratios (at 355 and 532 nm) that we obtain from all the combinations of the real and imaginary parts for each effective radius tested in this sensitivity study.

The extinction-related Ångström exponents largely reflect our experience we gained from measurements of extinction coefficients at 355 and 532 nm. We regularly measure extinction-related Ångström exponents of 1–2 in regions that are affected by an-

thropogenic pollution. Maximum values that have been measured are as high as 2.5 but we did not test this scenario in our study.

Values below 1 describe large particles in the coarse mode fraction. The most likely candidate of an aerosol type with extinction-related Ångström exponents below 1 is mineral dust. However, we cannot simulate with reasonable confidence optical data that describe mineral dust particles. Until now we could not identify a light-scattering model that would allow us to model trustworthy values of particle backscatter coefficients, i.e., scattering at 180°. However, we measured in the past extinction-related Ångström exponents of 0.5–1 which are related to aged biomass-burning aerosols (Müller et al., 2005). In a few instances extinction-related Ångström exponents of aged biomass-burning aerosols were less than 0.5.

We also considered the case of extinction-related Ångström exponents around 0. Again, this scenario most likely occurs if large mineral dust particles are present. However, also large sea-salt particles may show extinction-related Ångström exponents of around 0 and for that reason we simulated such cases as well. We point out that it is not unlikely to find extinction-related Ångström exponents slightly less than 0, as shown in Table 2. It is unclear if negative values can be resolved by lidar measurements in view of realistic measurement errors of 10–20 %.

The critical point in this table are the lidar ratios. Several values quite obviously are very unusual. Some lidar ratios are considerably higher than 100 sr, and some values are considerably lower than 20 sr. Lidar ratios of approximately 100 sr describe strong light-absorbing aerosols and lidar ratios around 20 sr describe non-absorbing sea salt. There remains the question if it is justified to simulate scenarios in which lidar ratios considerably exceed 100 sr respectively drop below 20 sr. We believe that we should consider such extreme outliers in at least a few studies for two reasons. First, we can test the robustness of our algorithms for such extreme cases. If we learn how the inversion algorithms behave in such cases we have the confidence that we could analyze aerosol scenarios in which the measured optical parameters might be outside the commonly accepted range of values for lidar ratios and Ångström exponents. The second

EARLINET inversion algorithms

D. Müller et al.

Title Page

Abstract

Introduction

Conclusions

References

Tables

Figures

|◀

▶|

◀

▶

Back

Close

Full Screen / Esc

Printer-friendly Version

Interactive Discussion



point is that the underlying microphysical properties do not seem to be completely out of range of numbers we can expect for atmospheric particles. It is simply the combination of specific values of particle size distribution and CRI that creates the outliers of lidar ratios.

5 3.2 Simulation results of TROPOS/UH algorithm

We carried out the inversions as described in the methodology section. We tested how well we can retrieve the parameters of interest under favorable circumstances. In this study we define favorable circumstances as the situation in which we have approximate knowledge of the real part of the complex refractive index. This latter assumption is 10 based on a recent study by Chemyakin et al. (2014) who show that the “Arrange and Average” Algorithm may be a method that could allow us to constrain the real part of the refractive index to 0.1 or even 0.05 uncertainty; see Table 3 in Chemyakin et al. (2014). We made use of this possibility in this study. We explicitly did not attempt to further optimize our inversion results by selecting a subset of best possible solutions 15 in the sense of manually selecting solutions from the solution space that follows from constraining the real part to either 0.05 or 0.1. We obtain a family of individual solutions for which the real part is within either 0.1 or 0.05 deviation from the true value. We average this family of solutions and thus obtain mean value and uncertainty, which in this study will be expressed in terms of accuracy (systematic error or bias) and 20 precision (statistical error or noise).

We also tested our algorithm under the assumption of comparably unfavorable measurement error scenarios. We distorted each optical data point by its maximum value of either 5, 10, or 15 %. In that regard errors of 15 % represent the worst case scenario in this study. We did this distortion without considering the possibility that data points 25 may be correlated to each other and thus error bars may also not be independent of each other. We assume that the inversion of such “extremely” distorted backscatter and extinction spectra would result in microphysical parameters that also deviate to a maximum value from the correct values. This assumption of course has the flaw that

Title Page	
Abstract	Introduction
Conclusions	References
Tables	Figures
	
	
Back	Close
Full Screen / Esc	
Printer-friendly Version	
Interactive Discussion	



[Title Page](#)[Abstract](#)[Introduction](#)[Conclusions](#)[References](#)[Tables](#)[Figures](#)[|◀](#)[▶|](#)[◀](#)[▶](#)[Back](#)[Close](#)[Full Screen / Esc](#)[Printer-friendly Version](#)[Interactive Discussion](#)

the inversion is a non-linear problem. That means, an extreme distortion of optical input data may not necessarily need to lead to a maximum deviation of the retrieved micro-physical parameters from their true values. However, we believe that we will learn more about this type of error analysis in this first attempt and that we can refine it in future studies.

3.2.1 Results for error cases 0 and 15%

Figure 5 shows a summary of the retrieval performance of effective radius, number, surface-area, and volume concentration, and the real and imaginary part we obtain with the TROPOS/UH algorithm. The left panel shows the results of simulations carried out for error free data. The right panel shows the extreme error estimation of the retrieval results.

According to (Chemyakin et al., 2014) the real part of the CRI of the optical data used in this study can be retrieved to an accuracy of approximately 0.1 with 2σ confidence for the case of noiseless optical data, see Table 3 in Chemyakin et al. (2014). We made use of this result in our simulations as we are mainly interested in finding out about the performance of the algorithm under favorable condition of input parameters and constraints to the search space of the refractive index grid which poses the greatest challenge in our retrieval algorithm. If we learn more about the impact of the refractive index search grid we hope to learn more about how to modify our algorithm in order to improve the overall retrieval performance for all parameters investigated in this study.

Under this assumption of known refractive index the other parameters then can be derived accordingly. These results are shown as squares. We see that effective radius can be derived to high accuracy if particles are in the fine mode fraction. With regard to particles in the intermediate state (transition from fine mode to coarse mode, i.e., effective radii of 0.28 and 0.4 μm) and the coarse mode the performance on average still is acceptable (in view of the uncertainty bars) although we find outliers for particles with real parts of 1.4.

EARLINET inversion algorithms

D. Müller et al.

[Title Page](#)[Abstract](#)[Introduction](#)[Conclusions](#)[References](#)[Tables](#)[Figures](#)[|◀](#)[▶|](#)[◀](#)[▶](#)[Back](#)[Close](#)[Full Screen / Esc](#)[Printer-friendly Version](#)[Interactive Discussion](#)

that stepsize likely is a reason for the overestimation of the mean imaginary part (in the retrieval), which in turn leads to an underestimation of the single-scattering albedo for low light-absorbing aerosols particles.

Figure 5 also shows results if we assume that we could retrieve the real part to an accuracy of 0.05 (open circles). In that case we again make use of the results published by Chemyakin et al. (2014) who show that an uncertainty of 0.05 is possible with 1σ confidence if the “Arrange and Average” Algorithm is applied.

We obtained the results by selecting only those individual solutions for which the real part deviates less than 0.05 from the true value. The microphysical properties do not differ significantly from the results if the real part is retrieved to 0.1 accuracy, if we take account of the overall uncertainties of our inversion results. I.e., any attempts to further improve the real part retrieval may not necessarily result in significant improvements of other data products and we consider this an important outcome of our study.

With regard to single-scattering albedo Fig. 5 shows the results for each case separately, i.e., each case of true imaginary part contains 5 different cases (corresponding to the 5 different particle size distributions tested in the simulations). The true value of each of the cases is shown by a thick horizontal line. The color of each of these horizontal lines corresponds to the same color of the symbols that represent the inversion results for a given set of optical data.

The retrieved single-scattering albedo on average can be derived to within ± 0.05 regardless whether the real part is known to within 0.05 or 0.1. If single-scattering albedo is larger than 0.9, the inversion results become worse and tend to underestimate the true single-scattering albedo. Particularly, if the true single-scattering albedo is 1, the retrieved value is around 0.95.

With regard to measurement errors of the optical input data we carried out numerous simulation studies in the past (Müller et al., 1999b; Veselovskii et al., 2002, 2004). We also learnt about the impact of measurement errors from the analysis of experimental data. We know that on average measurement uncertainties should be less than 20 % in order to obtain microphysical parameters with low uncertainty. One point we are

EARLINET inversion algorithms

D. Müller et al.

[Title Page](#)

[Abstract](#) [Introduction](#)

[Conclusions](#) [References](#)

[Tables](#) [Figures](#)

[◀](#) [▶](#)

[◀](#) [▶](#)

[Back](#) [Close](#)

[Full Screen / Esc](#)

[Printer-friendly Version](#)

[Interactive Discussion](#)



struggling with is that uncertainty needs to be expressed in terms of accuracy and precision. All previous studies were only designed to estimate the uncertainty and we kept our studies fairly simple with respect to error analysis of the inversion results. We did not separately study systematic and statistical errors.

In this study we made the first step toward refining our error analysis. We used 5, 10, and 15 % noise for each optical data point. We wanted to test by how much the microphysical parameters could shift for a given measurement uncertainty. In this study we are mainly interested in the likely maximum shift of the mean value of each data product. We try to provide a first answer to that question by what we call extreme error estimation.

We distorted the backscatter and extinction spectra to their extreme and took the average of the extreme error runs as the final inversion result. For example we added 15 % to the extinction coefficient measured at 355 nm and we subtracted 15 % from the extinction coefficient at 532 nm. We did not apply any smoothing constraints that would reduce these extreme slopes of the extinction and backscatter spectra, and thus we also create extreme values of the extinction- and backscatter- and lidar-ratio-related Ångström exponents.

Another idea behind this approach of using maximum distortion is to find out what could possibly go wrong in data inversion if we do not know the error model that describes the uncertainty bars of the optical input data. For example we need to know how systematic and statistical error are computed from the Raman lidar data, as this definition would allow us to compute the uncertainty bars of the microphysical parameters in a more refined way. We need to know, if a Gauss-like error distribution function sufficiently well describes the error bars of the optical input data, or if a different error distribution function is more appropriate. We emphasize that error distribution functions contain information that can be used in data inversion as additional piece of constrain that might help us to improve the inversion results.

Our procedure needs to be taken with caution. It is just the first step toward dealing with the concept of error analysis in a more concise way. For example, we applied

EARLINET inversion algorithms

D. Müller et al.

Title Page

Abstract

Introduction

Conclusions

References

Tables

Figures

◀

▶

◀

▶

Back

Close

Full Screen / Esc

Printer-friendly Version

Interactive Discussion



Title Page	
Abstract	Introduction
Conclusions	References
Tables	Figures
	
Back	Close
Full Screen / Esc	
Printer-friendly Version	
Interactive Discussion	



the noise for each data point individually, i.e., we did not consider that errors of the individual data points of a given $3\beta + 2\alpha$ data set may be correlated to each other. Such an effect would likely have a significant impact on the inversion results. We also did not take account of the situation that certain situations of distorted data (i.e. values of Ångström exponents) may be less likely than other situations. We would like to use these results as motivation regarding the need for clearly defined data-analysis protocols, because the quality of the optical data significantly impacts the quality of the microphysical parameters, or in other words: if the input optical data do not meet certain quality standards, the inversion algorithms cannot fix that problem.

In the following we only discuss the results for 15 % error, see right panel of Fig. 5. 15 % error mainly disrupts the retrieval results if lidar ratios are above 100 sr, regardless of particle size and the real part. We notice that the effect is particularly pronounced for imaginary parts of 0.03 and 0.05. We find that a systematic shift could occur (loss of accuracy), but it would not necessarily lead to a change of the statistical uncertainty (loss of precision).

This effect of the loss of accuracy is obvious for effective radius and the uncertainties could become unacceptably large for some of the retrieved effective radii if we do not use other types of information to constrain the results, or if we do not know the mathematical function that describes the error bars.

Surface-area concentration remains within a reasonable range of uncertainty if we use 50 % as benchmark. It remains rather well behaved for the two PSDs that describe fine-mode particles, but also the other types of PSDs, i.e., the transition type and the coarse-mode type still deliver useful results.

Volume concentration shows reasonable results (we use around 50 % error as benchmark when we talk about useful results) for all imaginary parts except the value $0.05i$. The results worsen for large particles, i.e., for effective radii of $0.57 \mu\text{m}$, but we would be able to identify measurement situations in which coarse-mode particles dominate. We measure the extinction-related Ångström exponent, and large particles are

EARLINET inversion algorithms

D. Müller et al.

[Title Page](#)[Abstract](#)[Introduction](#)[Conclusions](#)[References](#)[Tables](#)[Figures](#)[◀](#)[▶](#)[◀](#)[▶](#)[Back](#)[Close](#)[Full Screen / Esc](#)[Printer-friendly Version](#)[Interactive Discussion](#)

linked to low Ångström exponents. Thus we can use the values from extinction measurements at two wavelengths as quality flag parameter of the inversion results.

The imaginary part is our main target of future studies as it allows us to derive light-absorption coefficients of particles. We find that the uncertainty (variation) of the imaginary parts that we obtain from erroneous data largely does not differ from the results of error free data. The exception are high imaginary parts ($0.05i$). In that case there is a high probability that we would systematically underestimate the imaginary part, if the error model is not known.

We find on average that single-scattering albedo is underestimated, regardless of the true value of the single-scattering albedo. We do not see a significant difference between the results for single-scattering albedo at 355 nm and single-scattering albedo at 532 nm.

3.2.2 Results in terms of correlation plots

Figure 6 presents the inversion results in terms of correlation plots. This representation allows for easier identification of the general performance of the inversion algorithm. The left panel of Fig. 6 shows the results for error-free optical data, the right panel shows the results for optical data errors of 15 %. The left column of each panel shows the results if the real part is known to 0.05. The right panel shows the results if the real part is known to 0.1.

The main results were already discussed in the context of Fig. 5. We find that on average the results slightly worsen if the real part is known to 0.1 instead of 0.05 accuracy. Figure 5i and j clearly shows the overestimation of the retrieved imaginary part if the true value drops below $0.01i$. Single-scattering albedo accordingly is underestimated, and this underestimation becomes quite apparent if the true single-scattering albedo rises above 0.95.

If we introduce errors in the optical data the quality of the inversion results worsens. Our approach of creating an extreme distortion of the optical spectra gives us some insight into the maximum uncertainties that may occur. We find that effective radius

[Title Page](#)[Abstract](#)[Introduction](#)[Conclusions](#)[References](#)[Tables](#)[Figures](#)[◀](#)[▶](#)[◀](#)[▶](#)[Back](#)[Close](#)[Full Screen / Esc](#)[Printer-friendly Version](#)[Interactive Discussion](#)

and volume concentration may exceed 50 % uncertainty. Surface-area concentration in most cases stays within ± 50 % uncertainty. The imaginary part interestingly stays within ± 50 % uncertainty if the true value is above $0.01i$. If the true value is below $0.01i$ the retrieved imaginary part may show a positive bias of 0.01 to 0.02. Regardless of the increased uncertainty of the microphysical properties single-scattering albedo still can be derived to ± 0.05 in many cases. However, as noted before (see Fig. 5) single-scattering albedo is on average underestimated.

3.2.3 Results in terms of accumulative distributions and comparison to results from UP algorithm

Figure 7 shows the accumulative distribution, i.e., the number of case studies for which each of the investigated parameters deviates less than a given value (shown on the x axis of each plot). We also compare our results to the ones obtained with the UP algorithm, see Fig. 7 (second panel).

With respect to effective radius the solid horizontal line shows that approximately 50 % of all solutions show less than 5–8 % deviation from the true results. We find that 75 % of all solutions have uncertainties of less than 15 % and that all solutions deviate less than 50 % from the true results.

If uncertainties of the optical data are 15 % only 50 % of all solutions may have errors less than 50 %, and uncertainties of the other 50 % of the solutions may have considerably larger uncertainties. We note that this is an extreme estimate, as we distorted the optical backscatter and extinction spectra to the maximum.

In the case of surface-area concentration 75 % of all simulated cases deviate less than 10 % from the true results, regardless if the real part is known to 0.05 or 0.1 accuracy. If we introduce uncertainties we find that 75 % of all solutions deviate less than 20 % from the true results.

In the case of volume concentration we find that 50 % of all solutions deviate less than 10 % from the true values. 75 % of all cases deviate less than 20 % from the true values and in 90 % of all simulated cases the retrieval error is less than 50 %. If we

EARLINET inversion algorithms

D. Müller et al.

[Title Page](#)[Abstract](#)[Introduction](#)[Conclusions](#)[References](#)[Tables](#)[Figures](#)[◀](#)[▶](#)[◀](#)[▶](#)[Back](#)[Close](#)[Full Screen / Esc](#)[Printer-friendly Version](#)[Interactive Discussion](#)

assume uncertainties of 15 % for the optical data, volume concentration may deviate less than 20 % from the true value in 50 % of all simulation cases.

With respect to the imaginary part the deviation is less than approximately 0.006 in 75 % of all cases. If measurement errors are included the deviation is ≤ 0.01 in 75 % of all cases.
5

Single-scattering albedo at 355 and 532 nm can be derived to better than 0.04 in 75 % of all cases if the real part is known to 0.05–0.1. In 90 % of all simulation cases we can retrieve single-scattering albedo to better than 0.06. If we introduce measurement errors the uncertainty of single-scattering albedo is ≤ 0.06 in 50 % of all cases and
10 ≤ 0.08 in 75 % of all cases.

3.3 Simulation results of UP algorithm

We split the discussion of our results into two parts: the first part deals with the results obtained with noiseless data. The second part deals with the case of noisy data. Moreover, we note that the complete evaluation is done without any restriction and
15 constraints with respect to the real part of the CRI as it was used previously for the evaluation of the TROPOS/UH algorithm.

3.3.1 The noiseless data case

First, we evaluate the effective radius retrieval and the retrievals of total surface-area and volume concentration. In case of noiseless input data, for almost all fine-mode
20 particle examples ($\sigma = 1.5, 1.7$) the effective radius can be retrieved with a relative error less than 7.5 % except for CRI $1.6+0i$, $1.6+0.05i$ with $\sigma = 1.5$ (not shown here) and for CRI $1.5+0.03i$, $1.5+0.05i$, $1.6+0.03i$, $1.6+0.05i$, i.e., for strong-absorbing particles, with $\sigma = 1.7$, see Fig. 8c. In that case the relative error is less than 10 %.

For almost all fine-coarse-mode and coarse-mode particles ($\sigma = 2.1, 2.3$), the effective radius is underestimated, see Fig. 8a. The underestimation is between 2 and 13 %. We find outliers for coarse-mode particles $\sigma = 2.3$ with CRI $1.4+0i$, $1.5+0i$ and $1.6+0i$,
25

EARLINET inversion algorithms

D. Müller et al.

[Title Page](#)[Abstract](#)[Introduction](#)[Conclusions](#)[References](#)[Tables](#)[Figures](#)[◀](#)[▶](#)[Back](#)[Close](#)[Full Screen / Esc](#)[Printer-friendly Version](#)[Interactive Discussion](#)

i.e., non-absorbing particles. The accuracy of the retrieved effective radius is here only about 25 %. But in 90 % of all simulation examples, the retrieval errors are below 13 %, see Fig. 7b.

The total surface-area and volume concentrations are two very stable microphysical parameters. Almost all cases can be retrieved to better than 15 %, ranging from nearly 0 to 15 %. For the first parameter, there are only two outliers for $\sigma = 1.5$ with CRI $1.4 + 0.01i$ and $1.4 + 0.03i$. In case of volume concentration we find 6 outliers. 5 of the outliers have real part 1.4. In almost all cases, the surface-area concentration is overestimated for $\sigma = 1.5, 1.9, 2.1$, see Fig. 8d. The volume concentration shows a very stable behavior, see Fig. 8g. In summary, 96 % of all examples with respect to total surface-area concentration and 90 % of all examples with respect to total volume concentration result in retrieval errors well below 15 %, see Fig. 7d and f.

Second, we evaluate the retrieval of the CRI. The retrieval of the real part is very stable, in particular for 1.5, see Fig. 10a and c, the relative error is below 3 % except for two outliers (not shown here). In summary, the relative error is below 5 % for all real parts and all simulation examples (two outliers) and the absolute deviation (90 % of all examples) is below 0.06, see Figs. 9b and 7h, respectively.

The imaginary part has a larger variation if the particles are more absorbing, see Fig. 10d. This result holds true for all real parts and is more pronounced for real part 1.4. The error bars are larger (standard deviation of all selected CRI grid points from the mean). Moreover, for the real part 1.4 (except 1 outlier) the imaginary part is always overestimated for strong-absorbing particles.

The relative error is less than 55 % except for 8 outliers which for most part have an imaginary part of $0.01i$. At the moment the reason for this behavior is unknown.

However, in summary, with respect to the imaginary part 83 % of all examples show retrieval errors below 50, and 94 % of all investigated imaginary parts show retrieval errors below 70 %, see Fig. 9b. We note that we do not include non-absorbing particles with $0i$ for our evaluation of the relative error since division by zero fails. Figure 10d shows that both the absolute deviation from zero and the error bars are very small.

Concerning the absolute error 70 % of all examples are below 0.005 absolute deviation and 85 % are below 0.01, see Fig. 7j.

3.3.2 The noisy data case

In the case of noisy input data (15 %), the relative error of the effective radius is monotonically decreasing with the real part of the CRI, i.e., for real part 1.4 the relative error is less than 60 %, for 1.5 it is less than 40 % and for 1.6 it is less than 30 %. For real part 1.4 the effective radius is overestimated in all examples of investigated PSDs. For the real parts 1.5 and 1.6 this overestimation still occurs in the case of the fine-mode particles, see Fig. 8b. It is worth mentioning that the relative errors for fine-mode particles are for the most part larger than for the intermediate and coarse-mode particles. In summary, 85 % of all investigated examples show retrieval errors below 50 %, see Fig. 7b. However, by including only the real parts 1.5 and 1.6, 98 % of all examples show retrieval errors below 40 %.

The surface-area concentration is the most stable parameter in the case of noisy data. The retrieval error is less than 20 % (1 outlier) with respect to real part 1.4. In the case of real parts 1.5 and 1.6 the retrieval error is less than 15 % (2 outliers). The parameter is slightly overestimated for fine-coarse- and coarse-mode particles, see Fig. 8e, but stays within the error bars. The retrieval for fine-mode particles is excellent for real parts 1.5 and 1.6 and all imaginary parts. In summary, 99 % of all investigated examples show retrieval errors below 20 and 85 % of all investigated examples show retrieval errors below 15 %, see Fig. 7d. We note that the retrieval error for most of the examples does not exceed the level of the input data error.

The volume concentration is also slightly overestimated, but in contrast to surface-area concentration this is for the most part only happening for fine-mode particles, see Fig. 8h. The overestimation stays mostly within the error bars for real parts 1.5 and 1.6. Moreover, volume concentration is overestimated for all particles with real part 1.4. The retrieval error is less than 35 % for real parts 1.5 and 1.6. This means, that on average it stays within the input data error level. For the real part 1.4 the volume concentration

Title Page

Abstract

Introduction

Conclusions

References

Tables

Figures

◀

▶

◀

▶

Back

Close

Full Screen / Esc

Printer-friendly Version

Interactive Discussion



has a retrieval error less than 55 % except for $\sigma = 2.1, 2.3$ where it is 70 %. For fine-mode particles the volume concentration has a retrieval error less than 40 % for all CRI. In summary, 88 % of all investigated examples have a retrieval error below 50 % with respect to the volume concentration, see Fig. 7f. However, if we consider only real parts 1.5 and 1.6 the retrieval error is below 40 % in 100 % of those examples.
5

In contrast to the noiseless data case, the real part of CRI 1.4 is always underestimated (1 outlier) in the case of noisy data, see Fig. 10b. Moreover, it is nearly always (all real parts) underestimated for fine-mode particles and the relative error is larger than for intermediate and coarse-mode particles. But the retrieval error is still very
10 small, i.e., 89 % of all examples are below 5 and 100 % of all examples are below 6 % retrieval error. With respect to the absolute deviation 85 % (noiseless case) and 65 % (noisy case), respectively, are below ± 0.05 and 100 % (in both cases, two outliers) are well below ± 0.1 , see Fig. 7h.

Concerning the imaginary part of CRI we found that the error bars are very large for
15 strong-absorbing particles (precision is low), i.e., imaginary parts $0.03i$ and $0.05i$, see Fig. 10e. But for non- and weak-absorbing particles the accuracy and precision is good. In summary, 90 % of all investigated examples are below 40, 93 % are below 50, and 100 % (only 2 outliers) are below 60 % retrieval error, see Fig. 9b. Notice again, that non-absorbing particles with $0i$ are not included here for the relative error evaluation.
20 But one can see from Fig. 10e that the absolute deviation as well as the error bars are very small for non-absorbing particles.

In detail, as already remarked above, if we want to obtain an absolute accuracy of approximately ± 0.03 for the SSA, which is a basic requirement for climate change studies, one needs to test if it is possible to retrieve the imaginary part of CRI within
25 ± 0.005 in absolute values. We found that for non- ($0i$) and weak-absorbing ($0.005i$, $0.01i$) particles this is possible, i.e., accuracy ± 0.005 in absolute values is achievable; for real part 1.6 it seems to be even possible for strong-absorbing particles ($0.03i$, $0.05i$), see Fig. 9a. For the rest of strong-absorbing cases the absolute error stays within ± 0.015 except two outliers. In summary, 82 % of all examples stay below ± 0.005

Title Page	
Abstract	Introduction
Conclusions	References
Tables	Figures
	
	
Back	Close
Full Screen / Esc	
Printer-friendly Version	
Interactive Discussion	



and 92 % below ± 0.01 absolute retrieval error, see Fig. 7j. A closer look to Figs. 7j and 9a shows that for the imaginary part, the noisy data case delivers better results than the noiseless one. This fact needs further investigation in future.

3.3.3 Evaluation results for SSA

- 5 Here we evaluate the accuracy of single-scattering albedo for the noiseless and noisy case. As expected from the absolute retrieval error of the imaginary part of the CRI – which is larger for strong-absorbing particles – the single-scattering albedo at 355 and 532 nm shows more or less the same behavior in the noiseless and noisy case, respectively, see Figs. 9d–f and 11a, b, d, e. For noiseless data, 91 % of all examples (355 and 532 nm) are below 6 % retrieval error. 99 % of all examples at 355 nm and 95 % of all examples at 532 nm are below 10 % retrieval error, see Fig. 9c. With respect to 15 % noisy data, we found that 100 % of all examples achieve retrieval errors below 12 % for the single-scattering albedo at 355 and 532 nm. In more detail, the SSA retrieval errors are well below 6 % in 87 % of all examples at the wavelength 355 nm or in 88 % of all examples at the wavelength 532 nm, respectively, see Fig. 9c.
- 10
- 15

Regarding the absolute deviation and the cases of noiseless input data we found an underestimation of SSA at 355 nm (and similar for SSA at 532 nm) for non- and weak-absorbing particles in the intermediate and coarse-mode. For non- and weak-absorbing particles in the fine-mode the accuracy limit of ± 0.03 (in absolute values) is achieved, see Fig. 9d. In the noisy data case this underestimation (in the intermediate and coarse-mode) of SSA at 355 and 532 nm only occurs for all imaginary parts at real part 1.4, see Fig. 9e and f. For nearly all non- and weak-absorbing particles with real parts 1.5 and 1.6 the accuracy limit ± 0.03 is achieved in all 5 modes at 532 nm whereas at 355 nm in such cases the accuracy limit is ± 0.05 (one outlier), see Fig. 9e and f. In summary, 70 % (65 %) of all examples stay below ± 0.03 for SSA at 532 nm ((at 355 nm) and 88 % of all examples (both wavelengths) stay below ± 0.05 , see Fig. 7l and n).

20

25

Title Page	
Abstract	Introduction
Conclusions	References
Tables	Figures
	
	
Full Screen / Esc	
Printer-friendly Version	
Interactive Discussion	



3.3.4 Results in dependence of increasing noise level

We complete the evaluation in showing how the retrieval error is increasing with respect to the noise level using one example namely fine-mode particles with gsd $\sigma = 1.7$. We investigated 0, 5, 10 and 15 % input noise. Figure 8c shows the retrieval error of the effective radius for increasing noise level. For the real part 1.4 we clearly see the expected behavior, i.e., the retrieval error increases with increasing noise level. The same is true for real part 1.5 and strong-absorbing particles. For all other CRI, the noise level seems to have less influence. Additionally, in Fig. 8c and i, one can see that for noiseless data one obtains very good retrieval results for the effective radius and for the volume concentration, more or less independently of the CRI. However, Fig. 8i shows that for the volume concentration the noise level itself seems to have nearly always only a minor impact on the results.

Although the surface-area concentration is a very stable parameter in the retrieval process, Fig. 8f shows surprisingly reverse results with respect to increasing noise level, in particular, for real parts 1.5 and 1.6.

The retrieval of the real part of the CRI, see Fig. 10c, shows more or less what one would expect for noiseless data. Whereas the noise level seems to be again less important for the relative retrieval error. In contrast the imaginary part of the CRI, see Fig. 10f, and the single-scattering albedo, see Fig. 11c and f, show no regular behavior even for noiseless input data, in particular, for strong-absorbing particles with respect to real parts 1.5 and 1.6. This behavior needs further examinations.

4 Summary

We summarize the status of two manually operated data inversion algorithms (TRO-POS/UH algorithm and UP algorithm) that are used to derive microphysical parameters of atmospheric particles observed with EARLINET multiwavelength ($3\beta + 2\alpha$) Raman lidar. The algorithms provide particle effective radius, and surface-area and volume

AMTD

8, 12823–12885, 2015

EARLINET inversion algorithms

D. Müller et al.

[Title Page](#)

[Abstract](#)

[Introduction](#)

[Conclusions](#)

[References](#)

[Tables](#)

[Figures](#)

◀

▶

◀

▶

[Back](#)

[Close](#)

[Full Screen / Esc](#)

[Printer-friendly Version](#)

[Interactive Discussion](#)



concentration, and the real and imaginary part of the complex refractive index. Single-scattering albedo can be computed from the derived particle size distributions and complex refractive indices with Mie-scattering algorithms.

4.1 TROPOS/UH algorithm

- 5 We tested the algorithms ability to derive the investigated particle parameters as accurately as possible, if the optical input data are error free and if the real part of the complex refractive index is known to 0.1, respectively 0.05 uncertainty. This latter assumption was introduced in our simulation study in view of results published by Che-myakin et al. (2014) who show that it may be possible to constrain the result for the
10 real part by the “Arrange and Average” Algorithm. We point out that this algorithm is currently further studied with respect to this interesting feature of being able to identify the real part of particles. Thus our own study can merely be considered as a first exploratory study, too. We also investigated the situation of noisy optical input data. In that regard we were not interested in investigating by how much we can compensate
15 for measurement errors in the inversion and still retrieve accurate microphysical particle properties. We were rather interested in the opposite goal: by how much can the derived microphysical parameters deviate from the true results, if a certain uncertainty level (5, 10, and 15 %) is reached. For that purpose we distorted the spectra of optical spectra (backscatter at 3 wavelengths and extinction at 2 wavelengths) to a maximum,
20 which likely will not occur under real experimental situations. We made the simplifying assumption that an extreme distortion of the optical input spectra leads to an extreme (maximum) deviation of the microphysical parameters from the true values. We acknowledge that this assumptions requires more studies to corroborate it.

25 We find that effective radius of the PSDs in the fine-mode, the intermediate case (fine and coarse mode particles), and the coarse-mode can be retrieved well. Accuracy usually is better than 25 % in all cases, though we notice outliers. Surface-area concentration can be retrieved with an accuracy of approximately 10 %. Statistical errors (precision) is just about large enough to include the true values, too. In most cases

Title Page	
Abstract	Introduction
Conclusions	References
Tables	Figures
	
	
Back	Close
Full Screen / Esc	
Printer-friendly Version	
Interactive Discussion	



we slightly underestimate the true values. Volume concentration can be retrieved well for the fine-mode, intermediate case, and coarse mode. Accuracy is better than 20% except for six outliers out of 75 investigated cases.

The real part was retrieved to either 0.1 or 0.05 uncertainty according to the methodology by Chemyakin et al. (2014), and thus is not part of the performance study of our inversion method.

It seems that the accuracy of the retrieved imaginary part in general is better than 30 % for all investigated cases if the true imaginary part is ≥ 0.1 . Taking into account precision (statistical error) we find that we still can derive the imaginary part to within $\pm 50\%$.

If the imaginary part is less than 0.01 we can merely decide if the mean value is ≤ 0.015 , and if we include statistical noise we lose precision as well. This results confirm previous, less systematic studies in which we found that we can merely determine the order of magnitude if the imaginary part is below 0.01.

Single-scattering albedo can be derived to approximately 0.05 in many of the investigated cases. Accuracy is in part better than 0.05, but if we include statistical errors we find deviations up to 0.1. These results however depend on the constraint of the real part. We find that if we can constraint the real part to 0.05, single-scattering albedo can be derived to better than 0.05 as long as its true value is ≤ 0.9 . We find a systematic underestimation of single-scattering if the true value is above 0.9. This effect is caused by the fact that our TROPOS/UH inversion method cannot accurately derive imaginary parts if they are less than 0.01. Particularly the fact that we cannot derive an imaginary part of 0 currently poses the greatest challenge.

We finally notice that it may not be so important for the retrieval quality of effective radius, and surface-area and volume concentration if the real part cannot be constrained to better than 0.1. Effects are more pronounced with regard to the imaginary part, though accuracy nearly always stays within $\pm 50\%$ as long as the true imaginary part is $\leq 50\%$. Below 0.1 (true) value the imaginary part is overestimated by on average 0.01. The quality of single-scattering albedo also depends on how accurate the real part can

EARLINET inversion algorithms

D. Müller et al.

Title Page

Abstract

Introduction

Conclusions

References

Tables

Figures

◀

▶

◀

▶

Back

Close

Full Screen / Esc

Printer-friendly Version

Interactive Discussion



be retrieved. If it can be retrieved to 0.05 we find that the retrieved single-scattering (at 355 and 532 nm) in nearly all investigated cases remains within 0.05 accuracy. Significant underestimation occurs if single-scattering albedo is above 0.9, as in that case the overestimation of the imaginary part plays a role. The quality of single-scattering albedo becomes notably worse if the real part is retrieved to only 0.1. In that case accuracy maybe be only 0.1.

With regard to our extreme error computations we find that results for the most part remain below 50 % accuracy and in many cases the accuracy is significantly better. We find outliers. We do not have sufficient information from this limited set of simulations that allows us to identify a pattern that could explain when the outliers occur. We believe that the inversion method is robust enough to provide microphysical size parameters with $\leq 50\%$ error(accuracy plus precision) even in cases of 15 % measurement error if the exact error-model of the optical uncertainty bar is unknown. We nevertheless emphasize that one goal of optical data analysis must be the characterization of the underlying error model of the optical data as it would likely improve significantly the microphysical inversion products.

With regard to the imaginary part we notice that on average the accuracy worsens with increasing noise level. We find more cases of overestimation respectively underestimation of the true imaginary part compared to the case of correct optical data. Results slightly differ if the real part is constrained to 0.05 respectively 0.1. However, if we take only results for which the true imaginary part is larger than 0.01, we still find that the retrieved imaginary parts are within $\pm 50\%$ from the true values.

Single-scattering albedo seems to be significantly underestimated compared to the results for single-scattering albedo in the case of noiseless optical data. Particularly we notice a wider scatter of values of single-scattering albedo around the true values. In contrast, in the case of noiseless optical input data the results for single-scattering albedo remain rather well confined within a narrow band of ± 0.05 deviation around the true values, except for the cases of single-scattering albedo ≥ 0.9 , see comments in Sect. 3.1.1.

Title Page	
Abstract	Introduction
Conclusions	References
Tables	Figures
◀	▶
◀	▶
Back	Close
Full Screen / Esc	
Printer-friendly Version	
Interactive Discussion	



4.2 UP algorithm

We summarize here our results of the UP algorithm for 15 % noisy input data.

The total surface area concentration is the most stable parameter within the microphysical retrieval procedure, i.e., 99 % of all examples are below 20 and 85 % are below 15 % retrieval error. The retrieval error level stays mostly within the input data error/noise level. With respect to the effective radius 85 % of all examples are below 50 % retrieval error. Additionally, by including only the real parts 1.5 and 1.6, 98 % of this examples are below 40 % retrieval error. For the total volume concentration we found 88 % of all examples are below 50 % retrieval error and, moreover, by including only real parts 1.5 and 1.6 the retrieval error stays below 40 % in 100 % of the examples.

We found for the imaginary part of the CRI that for non- ($0i$) and weak-absorbing ($0.005i$, $0.01i$) particles in all modes (fine, intermediate, coarse) the accuracy ± 0.005 in absolute values is achievable. For real part 1.6 it is on average even achievable for strong-absorbing particles ($0.03i$, $0.05i$). In summary, 82 % of all examples stay below ± 0.005 . Concerning the real part of CRI the relative retrieval error is very small, i.e., 100 % of all examples are below 6 % retrieval error. With respect to the absolute deviation 65 % of all examples are below ± 0.05 and 100 % are well below ± 0.1 .

The evaluation statistics show that the relative retrieval errors of effective radius and total volume concentration are prominently larger for the real part 1.4. The retrieval of the imaginary part of the CRI has significantly larger error bars for strongly light-absorbing particles of $0.03i$ and $0.05i$. The error bar behavior is monotonically increasing with an increasing light-absorption level. These observations are in agreement with mathematical theoretical studies which show that in general the degree of ill-posedness of the inverse problem grows both with increasing imaginary part and decreasing real part.

For fine-mode particles with gsd $\sigma = 1.5$ the relative retrieval errors of the effective radius and real part of the CRI are largest for almost all CRIs. The same is true for total surface area concentration but here only for real part 1.4, or for total volume con-

Title Page

Abstract

Introduction

Conclusions

References

Tables

Figures

◀

▶

Back

Close

Full Screen / Esc

Printer-friendly Version

Interactive Discussion



Title Page	
Abstract	Introduction
Conclusions	References
Tables	Figures
	
	
Full Screen / Esc	
Printer-friendly Version	
Interactive Discussion	

centration only for real part 1.6, respectively. For coarse-mode particles with $\sigma = 2.3$ the post-processing procedure is very complicated and time consuming since the CRI domain often has neither a diagonal structure nor any other well-defined domain. It is sometimes even speckled. Selecting the CRI associated with PSD may be difficult.

- 5 As expected from the absolute retrieval error of the imaginary part of the CRI, which is larger for strong absorbing particles, the single scattering albedo shows more or less the same behavior for 355 and 532 nm. For the single scattering albedo, 100 % of all examples achieve relative retrieval errors below 12 %. In more detail, 87 % of all examples for 355 nm and 88 % of all examples for 532 nm are well below 6 %. With
10 respect to the absolute error for nearly all non- and weak-absorbing particles with real parts 1.5 and 1.6 in all modes (fine, intermediate, coarse) the accuracy limit ± 0.03 is achieved which is a basic requirement for climate change studies. In summary, 70 % (65 %) of all examples stay below ± 0.03 for SSA 532 nm (355 nm).

5 Outlook

- 15 Future development work of the TROPOS/UH algorithm will focus on deriving fine mode and coarse mode particle parameters separately. We want to investigate in how far a wavelength-dependent complex refractive index of aerosol particles influences the quality of the retrieval results. Reason for this study is that we assume a wavelength-independent refractive index in our retrievals. We want to investigate if we can derive
20 the single-scattering albedo with less uncertainty if the true value of SSA is above 0.9.

In future the Potsdam group will improve the presented software in using the two regularization methods namely TSVD and iterative Pade method in parallel to utilize advantages of both methods simultaneously.

- Currently the Potsdam group is investigating in a microphysical retrieval procedure
25 via regularization for non-spherical particles, in particular, spheroidal particles, i.e., oblate and prolate particles. In future a user-friendly software tool for non-spherical could be developed.



EARLINET inversion algorithms

D. Müller et al.

Acknowledgements. This work has been supported since 2000 under Grant No. EVR1-CT-1999-40003's (EARLINET project) of the Environment Program of the European Union and Grant No. RICA-025991 (EARLINET-ASOS project) of the 6th Framework EU program. The work has been supported partially by the European Union Seventh Framework Program for research, technological development and demonstration under grant agreement No. 289923 – ITaRS and by DAAD project “Ostpartnerschaften” of Potsdam University.

References

- Alados-Arboledas, L., Müller, D., ad F. Navas-Guzmán, J. L. G.-R., Pérez-Ramírez, D., and Olmo, F. J.: Optical and microphysical properties of fresh biomass burning aerosol retrieved by Raman lidar, and star- and sun-photometry, *Geophys. Res. Lett.*, 38, L01807, doi:10.1029/2010GL045999, 2011. 12829
- Althausen, D., Müller, D., Ansmann, A., Wandinger, U., Hube, H., Clauder, E., and Zörner, S.: Scanning 6-wavelength 11-channel aerosol lidar, *J. Atmos. Ocean. Tech.*, 17, 1469–1482, 2000. 12827
- Amato, U., Carfora, M. F., Cuomo, V., and Serio, C.: Objective algorithms for the aerosol problem, *Appl. Optics*, 34, 5442–5452, 1995. 12834
- Ansmann, A. and Müller, D.: Lidar and atmospheric aerosol particles, in: *Lidar. Range-Resolved Optical Remote Sensing of the Atmosphere*, edited by: Weitkamp, C., Springer, New York, 105–141, 2005. 12831, 12851
- Böckmann, C.: Hybrid regularization method for the ill-posed inversion of multiwavelength lidar data to determine aerosol size distributions, *Appl. Optics*, 40, 1329–1342, 2001. 12829, 12830, 12831, 12839
- Böckmann, C. and Kirsche, A.: Iterative regularization method for lidar remote sensing, *Comput. Phys. Commun.*, 174, 607–615, 2006. 12830, 12841
- Böckmann, C. and Osterloh, L.: Runge–Kutta type regularization method for inversion of spheroidal particle distribution from limited optical data, *Inverse Probl. Sci. En.*, 22, 150–165, 2014. 12830
- Böckmann, C. and Pornsawad, P.: Iterative Runge–Kutta–type methods for nonlinear ill–posed problems, *Inverse Problems*, 24, 025002, 17 pp., doi:10.1088/0266-5611/24/2/025002, 2008. 12829

[Title Page](#)[Abstract](#)[Introduction](#)[Conclusions](#)[References](#)[Tables](#)[Figures](#)[|◀](#)[▶|](#)[◀](#)[▶](#)[Back](#)[Close](#)[Full Screen / Esc](#)[Printer-friendly Version](#)[Interactive Discussion](#)

- Böckmann, C. and Wauer, J.: The influence of spheroids on the inversion in the retrieval of microphysical particle parameters from lidar data, Proc. SPIE, 4150, 282–289, 2001a. 12830
- Böckmann, C. and Wauer, J.: Algorithms for the inversion of light scattering data from uniform and non-uniform particles, J. Aerosol Sci., 32, 49–61, 2001b. 12830
- 5 Böckmann, C., Mironova, I., Müller, D., Schneidenbach, L., and Nessler, R.: Microphysical aerosol parameters from multiwavelength lidar, J. Opt. Soc. Am. A, 22, 518–528, 2005. 12827, 12829, 12830, 12831
- 10 Böckmann, C., Osterloh, L., Rother, T., Serikov, I., Linne, H., and Kinne, S.: Optical and Microphysical Properties from Raman Lidar and Depolarization Data, p. 4, presented on 26th International Lidar Radar Conference, 25–29 June 2012, Porto Heli, Greece, 2012. 12831
- Bohren, C. F. and Huffman, D. R. (Eds.): Absorption and Scattering of Light by Small Particles, John Wiley, Hoboken, NJ, 1983. 12832
- 15 Chemyakin, E., Müller, D., Burton, S., Kolgotin, A., Hostetler, C., and Ferrare, R.: Arrange and average algorithm for the retrieval of aerosol parameters from multiwavelength highspectral-resolution lidar/Raman lidar data, Appl. Optics, 53, 7252–7266, 2005. 12849, 12850, 12851, 12852, 12863, 12864, 12881
- Engl, H. W., Hanke, M., and Neubauer, A.: Regularization of Inverse Problems Series: Mathematics and Its Applications, Vol. 375, Springer-Verlag, ISBN 978-0-7923-4157-4, 322 pp., 1996. 12833, 12834, 12839
- 20 Eixmann, R., Böckmann, C., Fay, B., Matthias, V., Mattis, I., Müller, D., Kreipl, S., Schneider, J., and Stohl, A.: Tropospheric aerosol layers after a cold front passage in January 2000 as observed at several stations of German Lidar Network, Atmos. Res., 63, 39–58, 2002. 12831
- Hansen, P. C.: Discrete Inverse Problems, Insight and Algorithms, SIAM, doi:10.1137/1.9780898718836, 213 pp., 2010. 12829, 12833, 12834, 12839, 12841
- 25 Heintzenberg, J., Müller, H., Quenzel, H., and Thomalla, E.: Information content of optical data with respect to aerosol properties: numerical studies with a randomized minimization-search-technique inversion algorithm, Appl. Optics, 20, 1308–1315, 1981. 12834
- Hoffmann, A., Osterloh, L., Stone, R., Lampert, A., Ritter, C., Stock, M., Tunved, P., Hennig, T., Böckmann, C., Li, S.-M., Eleftheriadis, K., Maturilli, M., Orgis, T., Herber, A., Neuber, R., and Dethloff, K.: Remote sensing and in-situ measurements of tropospheric aerosol, a PAMARCMiP case study, Atmos. Environ., 52, 56–66, 2012. 12831
- 30 Kirsche, A. and Böckmann, C.: Páde iteration method for regularization, Appl. Math. Comput., 180, 648–663, 2006. 12829, 12841

Title Page	
Abstract	Introduction
Conclusions	References
Tables	Figures
	
	
Full Screen / Esc	
Printer-friendly Version	
Interactive Discussion	



Müller, D., Wandinger, U., Althausen, D., Mattis, I., and Ansmann, A.: Retrieval of physical particle properties from lidar observations of extinction and backscatter at multiple wavelengths, *Appl. Optics*, 37, 2260–2263, 1998.

Müller, D., Wandinger, U., and Ansmann, A.: Microphysical particle parameters from extinction and backscatter lidar data by inversion with regularization: theory, *Appl. Optics*, 38, 2346–2357, 1999a. 12828, 12831, 12834, 12835, 12836

Müller, D., Wandinger, U., and Ansmann, A.: Microphysical particle parameters from extinction and backscatter lidar data by inversion with regularization: simulation, *Appl. Optics*, 38, 2358–2368, 1999b. 12828, 12834, 12836, 12851, 12852

Müller, D., Franke, K., Wagner, F., Althausen, D., Ansmann, A., Heintzenberg, J., and Verver, G.: Vertical profiling of optical and physical particle properties over the tropical Indian Ocean with six-wavelength lidar, 2. Case studies, *J. Geophys. Res.*, 106, 28577–28595, 2001a. 12828

Müller, D., Wandinger, U., Althausen, D., and Fiebig, M.: Comprehensive particle characterization from three-wavelength Raman-lidar observations, *Appl. Optics*, 40, 4863–4869, 2001b. 12827, 12828, 12851

Müller, D., Mattis, I., Wandinger, U., Ansmann, A., Althausen, D., and Stohl, A.: Raman lidar observations of aged Siberian and Canadian forest-fire smoke in the free troposphere over Germany in 2003: microphysical particle characterization, *J. Geophys. Res.*, 110, D17201, doi:10.1029/2004JD005756, 2005. 12828, 12829, 12848

Müller, D., Veselovskii, I., Kolgotin, A., Tesche, M., Ansmann, A., and Dubovik, O.: Vertical profiles of pure dust and mixed smoke-dust plumes inferred from inversion of multiwavelength Raman/polarization lidar data and comparison to AERONET retrievals and in situ observations, *Appl. Optics*, 52, 3178–3202, 2013. 12829

Noh, Y. M., Müller, D., Mattis, I., Lee, H., and Kim, Y. J.: Vertically resolved light-absorption characteristics and the influence of relative humidity on particle properties: multiwavelength Raman lidar observations of East Asian aerosol types over Korea, *J. Geophys. Res.*, 116, D06206, doi:10.1029/2010JD014873, 2011. 12828

Osterloh, L., Pérez, C., Böhme, D., Baldasano, J. M., Böckmann, C., Schneidenbach, L., and Vicente, D.: Parallel software for retrieval of aerosol distribution from LIDAR data in the framework of EARLINET-ASOS, *Comput. Phys. Commun.*, 180, 2095–2102, 2009. 12830, 12840

Osterloh, L., Böckmann, C., Mamouri, R.-E., and Papayannis, A.: An adaptive base point algorithm for the retrieval of aerosol microphysical properties, *Open Atmospheric Science Journal*, 5, 61–73, 2011. 12830, 12841

EARLINET inversion algorithms

D. Müller et al.

Title Page

Abstract

Introduction

Conclusions

References

Tables

Figures

◀

▶

◀

▶

Back

Close

Full Screen / Esc

Printer-friendly Version

Interactive Discussion



EARLINET inversion algorithms

D. Müller et al.

[Title Page](#)[Abstract](#)[Introduction](#)[Conclusions](#)[References](#)[Tables](#)[Figures](#)[◀](#)[▶](#)[◀](#)[▶](#)[Back](#)[Close](#)[Full Screen / Esc](#)[Printer-friendly Version](#)[Interactive Discussion](#)

Osterloh, L., Böckmann, C., Nicolae, D., and Nemuc, A.: Regularized inversion of microphysical atmospheric particle parameters: theory and application, *J. Comput. Phys.*, 237, 79–94, 2013. 12830, 12831, 12842

Papayannis, A., Mamouri, R. E., Nenes, A., Tsaknakis, G., Georgouassis, G., Avdikos, G., Böckmann, C., Osterloh, L., Eleftheriadis, K., Böhme, D., and Stohl, A.: Optical, microphysical and chemical properties of tropospheric aerosols retrieved by a 6-wavelength RAMAN lidar system during a biomass burning event over Athens, Greece, Proceeding of the 24th International laser radar conference, 381–384, Boulder, Colorado, USA, 23–27 June 2008. 12831

Phillips, D. L.: A technique for the numerical solution of certain integral equations of the first kind, *J. Assoc. Comput. Mach.*, 9, 84–97, 1962. 12834

Qing, P., Nakane, H., Sasano, Y., and Kitamura, S.: Numerical simulation of the retrieval of aerosol size distribution from multiwavelength laser radar measurements, *Appl. Optics*, 28, 5259–5265, 1989. 12826

Samaras, S., Nicolae, D., Böckmann, C., Vasilescu, J., Binietoglou, J., Labzovskii, L., Toanca, F., and Papayannis, A.: Using Raman-lidar-based regularized microphysical retrievals and aerosol mass spectrometer measurements for the characterization of biomass burning aerosols, *J. Comput. Phys.*, 299, 156–174, 2015. 12831, 12842, 12843, 12844

Tesche, M., Müller, D., Groß, S., Ansmann, A., Althausen, D., Freudenthaler, V., Weinzierl, B., Veira, A., and Petzold, A.: Optical and microphysical properties of smoke over Cape Verde inferred from multiwavelength lidar measurements, *Tellus B*, 63, 677–694, 2011. 12829

The EARLINET publishing group 2000–2010; Adam, M., Alados-Arboles, L., Althausen, D., Amiridis, V., Amodeo, A., Ansmann, A., Apituley, A., Arshinov, Y., Balis, D., Belegante, L., Bobrovnikov, S., Boselli, A., Bravo-Aranda, J. A., Bosenberg, J., Carstea, E., Chaikovsky, A., Comeron, A., D'Amico, G., Daou, D., Dreischuh, T., Engelmann, R., Finger, F., Freudenthaler, V., Garcia-Vicaino, D., Garcia, A. J. F., Geiss, A., Giannakaki, E., Giehl, H., Giunta, A., de Graaf, M., Granados-Munoz, M. J., Grein, M., Grigorov, I., Gross, S., Gruening, C., Guerrero-Rascado, J. L., Haefelin, M., Hayek, T., Iarlori, M., Kanitz, T., Kokkalis, P., Linne, H., Madonna, F., Mamouri, Rodanthi-Elisavet, Matthias, V., Mattis, I., Menendez, F. M., Mitev, V., Mona, L., Morille, Y., Munoz, C., Muller, A., Muller, D., Navas-Guzman, F., Nemuc, A., Nicolae, D., Pandolfi, M., Papayannis, A., Pappalardo, G., Pelon, J., Perrone, M. R., Pietruczuk, A., Pisani, G., Potma, C., Preissler, J., Pujadas, M., Putaud, J., Radu, C., Ravetta, F., Reigert, A., Rizi, V., Rocadenbosch, F., Rodriguez, A., Sauvage, L., Schmidt, J., Schnell, F., Schwarz, A.,

- Seifert, P., Serikov, I., Sicard, M., Silva, A. M., Simeonov, V., Siomos, N., Sirch, T., Spinelli, N., Stoyanov, D., Talianu, C., Tesche, M., De Tomasi, F., Trickl, T., Vaughan, G., Volten, H., Wagner, F., Wandinger, U., Wang, X., Wiegner, M., and Wilson, K. M.: EARLINET All Observations (2000–2010), World Data Center for Climate (WDCC), http://dx.doi.org/10.1594/WDCC/EN_all_measurements_2000-2010, 2014. 12830
- Tikhonov, A. N. and Arsenin, V. Y. (Eds.): *Solutions of Ill-posed Problems*, John Wiley, New York, 1977. 12827, 12834, 12835
- Twomey, S.: The application of numerical filtering to the solution of integral equations encountered in indirect sensing measurements, *J. Franklin Inst.*, 279, 95–109, 1965. 12833
- Twomey, S. (Eds.): *Introduction to the Mathematics of Inversion in Remote Sensing and Indirect Measurements*, Elsevier, Amsterdam, 1977. 12835, 12836
- Veselovskii, I., Kolgotin, A., Griaznov, V., Müller, D., Wandinger, U., and Whiteman, D. N.: Inversion with regularization for the retrieval of tropospheric aerosol parameters from multiwavelength lidar sounding, *Appl. Optics*, 41, 3685–3699, 2002. 12827, 12828, 12831, 12834, 12836, 12852
- Veselovskii, I., Kolgotin, A., Griaznov, V., Müller, D., Franke, K., and Whiteman, D. N.: Inversion of multiwavelength Raman lidar data for retrieval of bimodal aerosol size distribution, *Appl. Optics*, 43, 1180–1195, 2004. 12828, 12834, 12835, 12852
- Veselovskii, I., Dubovik, O., Kolgotin, A., Lapyonok, T., Girolamo, P. D., Summa, D., Whiteman, D. N., Mishchenko, M. I., and Tanré, D.: Application of randomly oriented spheroids for retrieval of dust particle parameters from multiwavelength lidar measurements, *J. Geophys. Res.*, 115, D21203, doi:10.1029/2010JD014139, 2010. 12829
- Wandinger, U. and Ansmann, A.: Experimental determination of the lidar overlap profile with Raman lidar, *Appl. Optics*, 41, 511–514, 2002. 12827
- Wandinger, U., Müller, D., Böckmann, C., Althausen, D., Matthias, V., Bösenberg, J., Weiß, V., Fiebig, M., Wendisch, M., Stohl, A., and Ansmann, A.: Optical and microphysical characterization of biomass-burning and industrial-pollution aerosols from multiwavelength lidar and aircraft measurements, *J. Geophys. Res.-Atmos.*, 107, 8125, doi:10.1029/2000JD000202, 2002. 12831
- Zuev, V. E. and Naats, I. E. (Eds.): *Inverse Problems of Lidar Sensing of the Atmosphere*, Springer, Berlin, 1983. 12833

EARLINET inversion algorithms

D. Müller et al.

[Title Page](#)

[Abstract](#)

[Introduction](#)

[Conclusions](#)

[References](#)

[Tables](#)

[Figures](#)

◀

▶

◀

▶

[Back](#)

[Close](#)

[Full Screen / Esc](#)

[Printer-friendly Version](#)

[Interactive Discussion](#)



**EARLINET inversion
algorithms**

D. Müller et al.

Table 1. Input parameters of the particle size distributions used in the simulation studies. We used monomodal PSDs with mean radius 100 nm. We used PSDs normalized to one particle per cm³. gsd (σ) denotes the geometric standard deviation (mode width). er is the effective radius, sc is the surface-area concentration, and vc the volume concentration.

gsd (μm)	er (μm)	sc ($\mu\text{m}^2 \mu\text{m}^{-3}$)	vc ($\mu\text{m}^2 \mu\text{m}^{-3}$)
1.5	0.15	0.18	0.0088
1.7	0.2	0.22	0.015
1.9	0.28	0.29	0.027
2.1	0.4	0.38	0.05
2.3	0.57	0.5	0.095

real part: 1.4, 1.5, 1.6
imaginary part: 0, 0.005, 0.01, 0.03, 0.05

Title Page	
Abstract	Introduction
Conclusions	References
Tables	Figures
Back	Close
Full Screen / Esc	
Printer-friendly Version	
Interactive Discussion	



EARLINET inversion
algorithms

D. Müller et al.

Title Page

Abstract

Introduction

Conclusions

References

Tables

Figures

◀

▶

◀

▶

Back

Close

Full Screen / Esc

Printer-friendly Version

Interactive Discussion



Table 2. Input parameters of the size distributions used in the simulation studies. We used monomodal PSDs with mean radius 100 nm. We used PSDs normalized to one particle per cm³. ext-A(355/532) denotes the extinction-related Ångström exponent for the wavelength pair 355/532 nm. bsc-A(355/532) and bsc-A(532/1064) denote the backscatter-related Ångström exponents for the wavelength pairs 355/532 nm and 532/1064 nm, respectively. LR(355) and LR(532) denote the lidar ratios at 355 and 532 nm, respectively. LR(532)/LR(355) denotes the color-ratio of the lidar ratios at 355 to 532 nm.

er (μm)	optical parameter	real part		
		1.4	1.5	1.6
0.15	ext-A(355/532)	1.45–1.78	1.29–1.49	1.09–1.23
	bsc-A(355/532)	0.36–1.38	0.53–1.79	1.06–2.37
	bsc-A(532/1064)	0.59–1.11	0.6–1.23	0.63–1.4
	LR(355)	81, 89, 99, 142, 191	55, 63, 11, 107, 153	34, 39, 44, 70, 106
	LR(532)	69, 73, 79, 101, 122	62, 67, 8, 92, 113	54, 59, 64, 84, 105
	LR(532)/LR(355)	0.64–0.85	0.74–1.13	0.99–1.59
0.2	ext-A(355/532)	0.94–1.11	0.73–0.85	0.54–0.59
	bsc-A(355/532)	0.19–1.19	0.61–1.76	1.16–2.12
	bsc-A(532/1064)	0.46–1.23	0.59–1.59	0.89–2.03
	LR(355)	72, 84, 96, 155, 229	34, 40, 47, 85, 138	16, 19, 23, 42, 72
	LR(532)	75, 82, 91, 129, 168	49, 55, 62, 95, 132	30, 34, 39, 62, 93
	LR(532)/LR(355)	0.73–1.03	0.96–1.45	1.29–1.86
0.28	ext-A(355/532)	0.55–0.62	0.37–0.4	0.23–0.24
	bsc-A(355/532)	0.03–1.08	0.48–1.31	0.75–1.47
	bsc-A(532/1064)	0.31–1.19	0.6–1.62	0.99–1.95
	LR(355)	56, 72, 87, 161, 257	23, 28, 34, 69, 124	10, 12, 15, 32, 59
	LR(532)	68, 79, 92, 146, 208	32, 39, 46, 81, 130	16, 19, 23, 43, 73
	LR(532)/LR(355)	0.81–1.21	1.05–1.44	1.24–1.64
0.4	ext-A(355/532)	0.3–0.32	0.16–0.17	0.07–0.08
	bsc-A(355/532)	-0.09–0.99	0.23–0.85	0.32–0.94
	bsc-A(532/1064)	0.17–1.1	0.5–1.31	0.78–1.48
	LR(355)	41, 60, 77, 163, 280	18, 24, 30, 64, 121	7, 10, 13, 29, 57
	LR(532)	54, 70, 85, 155, 239	23, 30, 36, 71, 124	10, 13, 17, 34, 63
	LR(532)/LR(355)	0.86–1.31	1.03–1.31	1.1–1.42
0.57	ext-A(355/532)	0.14	0.04–0.05	-0.01–0.02
	bsc-A(355/532)	-0.2–0.84	-0.03–0.51	-0.02–0.56
	bsc-A(532/1064)	0.04–1	0.31–0.94	0.46–1.04
	LR(355)	31, 52, 72, 169, 305	16, 22, 29, 65, 128	6, 9, 12, 30, 60
	LR(532)	41, 60, 78, 160, 265	19, 25, 32, 67, 123	8, 11, 14, 31, 60
	LR(532)/LR(355)	0.87–1.33	0.97–1.21	1–1.27

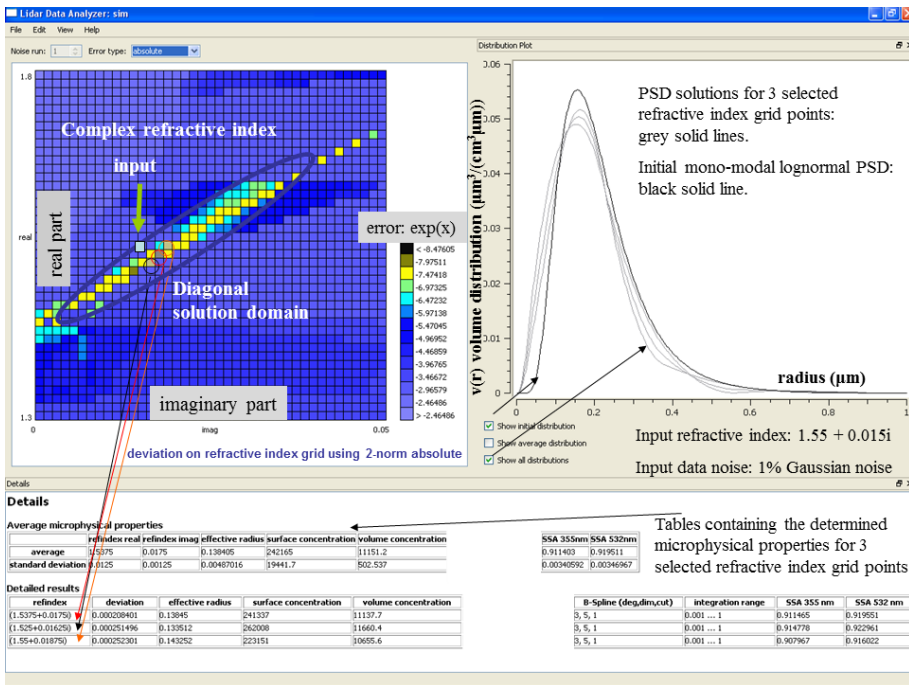


Figure 1. Screen shot of the developed software and explanation of the post-processing procedure: Selection of suitable grid points of CRI clustering along the diagonal domain (left), corresponding PSD and initial PDS (right), and tables with retrieved microphysical parameters for each selected CRI and mean values with standard deviation (bottom). The residual errors on the right hand side of the grid appear in ascending order from top to bottom on a logarithmic scale.

EARLINET inversion algorithms

D. Müller et al.

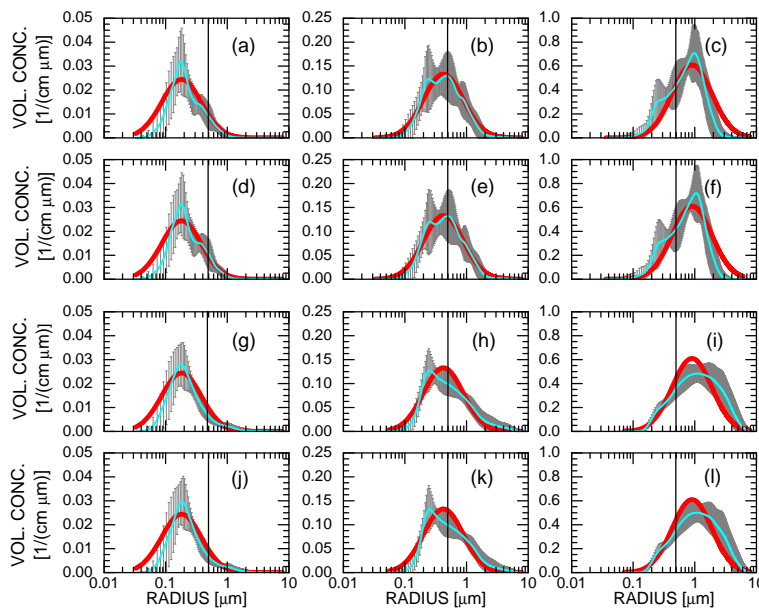


Figure 2. Examples of retrieved particle size distributions for the case of the geometric standard deviation of 2.1, real part of 1.5, imaginary part of $0.01i$ and for mean radius of **(a, d, g, j)** 60 nm, **(b, e, h, k)** 140 nm, and **(c, f, i, l)** 300 nm. The true PSD is shown as red curve. The retrieved mean PSDs are shown as solid, light-blue lines and error bars (grey) in terms of 1-sigma standard deviation. The error bars are plotted on a dense grid and follow from the averaging of several hundred individual inversion solutions for each of the mean PSDs. The vertical lines are positioned at 500 nm particle radius. We define 500 nm particle radius as separation between fine-mode and coarse mode particles. The four rows represent the two different constraints on the real part and error free data, i.e. 0.05 **(a–c)** and 0.1 **(d–f)**, rows **(g–i)** and **(j–l)** correspond to 15 % extreme optical data error.

[Title Page](#)[Abstract](#)[Introduction](#)[Conclusions](#)[References](#)[Tables](#)[Figures](#)[◀](#)[▶](#)[Back](#)[Close](#)[Full Screen / Esc](#)[Printer-friendly Version](#)[Interactive Discussion](#)

EARLINET inversion algorithms

D. Müller et al.

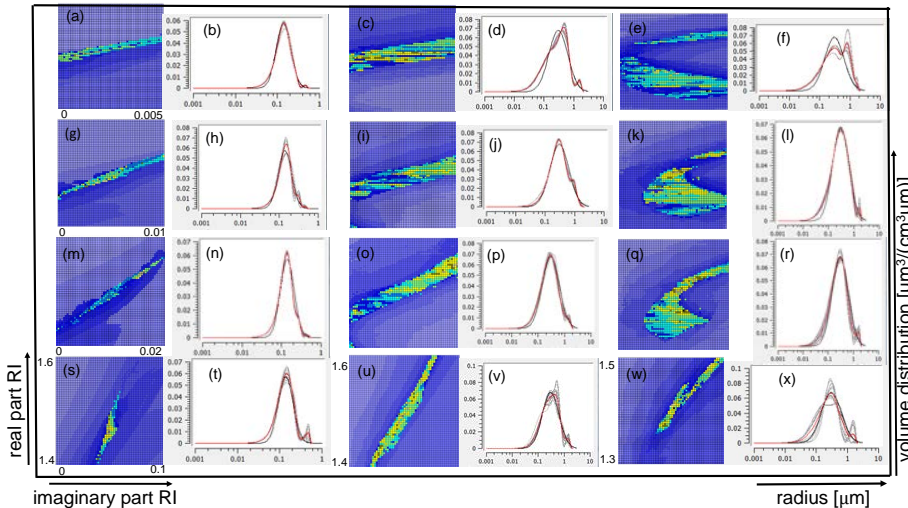


Figure 3. Examples of color-coded refractive index grids and PSDs for noiseless input data. The rows correspond to different imaginary parts of the CRI: 0, 0.005, 0.01 and 0.05. The first two columns contain fine-mode particles with $gsd \sigma = 1.5$ and real part of CRI 1.5 using equidistant B-spline nodes. The third and fourth columns correspond to intermediate-mode particles with $gsd \sigma = 2.1$ and real part of CRI 1.5 using non-equidistant B-spline nodes. The last two columns display results with $gsd \sigma = 2.1$ and real part of CRI 1.4 using equidistant B-spline nodes. The mean PSD (the solution) is drawn as red single line.

[Title Page](#)

[Abstract](#)

[Introduction](#)

[Conclusions](#)

[References](#)

[Tables](#)

[Figures](#)

◀

▶

[Back](#)

[Close](#)

[Full Screen / Esc](#)

[Printer-friendly Version](#)

[Interactive Discussion](#)



**EARLINET inversion
algorithms**

D. Müller et al.

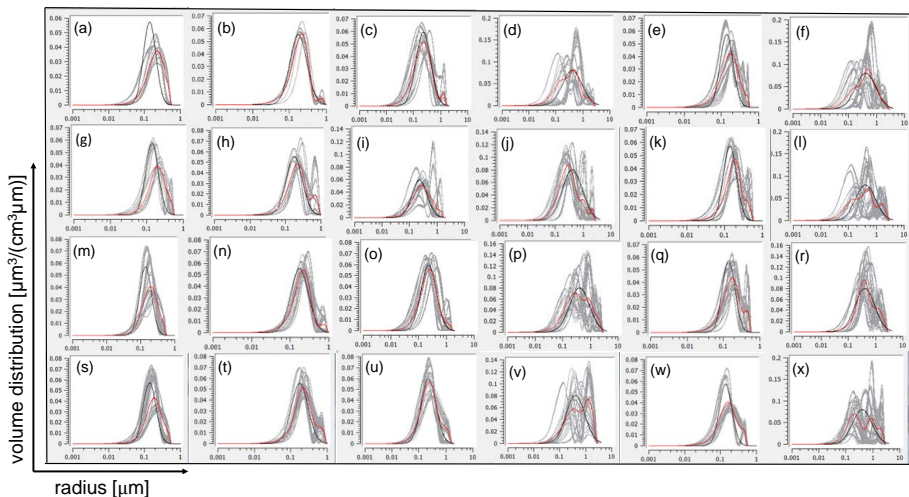


Figure 4. Examples of PSDs for input data with 15 % noise: the rows correspond to different imaginary parts of the CRI: 0, 0.005, 0.01 and 0.05. The columns correspond to gsd: 1.5, 1.7, 1.9, 2.3, 1.5, 2.3. The first four columns hold for real part 1.5. The last two columns describe the results for real part 1.6. The mean PSD, i.e., the solution, is shown as red single line.

[Title Page](#)[Abstract](#)[Introduction](#)[Conclusions](#)[References](#)[Tables](#)[Figures](#)[◀](#)[▶](#)[Back](#)[Close](#)[Full Screen / Esc](#)[Printer-friendly Version](#)[Interactive Discussion](#)

EARLINET inversion algorithms

D. Müller et al.

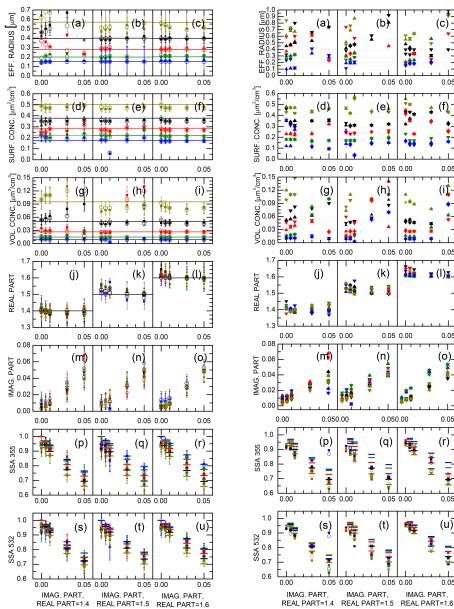


Figure 5. (left panel) TROPOS/UH algorithm: retrieval results for (a–c) effective radius, (d–f) surface-area concentration, (g–i) volume concentration, (j–l) real part and (m–o) imaginary part of the complex refractive index, and single-scattering albedo at (p–r) 355 nm and (s–u) 532 nm. The left segment shows the results for real part 1.4., the center segment shows the results for real part 1.5, and the right segment shows the results for real part 1.6. Our inversion results are obtained with an upper threshold of the real part of 0.1 (boxes) and a threshold of 0.05 accuracy (circles). The error bars denote one-standard deviation. (right panel) Results of our extreme error analysis for the case of 15 % measurement error. Upward-pointing triangles refer to results for which the real part was constrained to 0.05. Down-ward pointing triangles refer to inversion results for which the real part was constrained to 0.1. Meaning of the other symbols is the same as in the left panel.

[Title Page](#)

[Abstract](#)

[Introduction](#)

[Conclusions](#)

[References](#)

[Tables](#)

[Figures](#)

◀

▶

◀

▶

[Back](#)

[Close](#)

[Full Screen / Esc](#)

[Printer-friendly Version](#)

[Interactive Discussion](#)



EARLINET inversion algorithms

D. Müller et al.

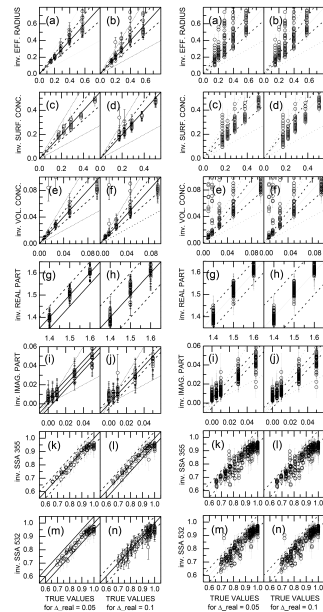


Figure 6. TROPOS/UH algorithm: (left panel) **(a, b)** effective radius, **(c, d)** surface-area concentration, **(e, f)** volume concentration, **(g, h)** real part and **(i, j)** imaginary part of the complex refractive index, and single-scattering albedo at **(k, l)** 355 nm and **(m, n)** 532 nm. (right panel) Retrieval results for the case of 15 % data uncertainty. The left (right) column in each of the two panels shows the results if the real part is known to an accuracy of 0.05 (0.1). The error bars denote one-standard deviation. The 1–1 lines are shown. The lines for $\pm 20\%$ deviation from the true results (dashed lines) and for $\pm 50\%$ deviation are shown for effective radius, and surface-area and volume concentration. In the case of the real part the dashed lines indicate ± 0.05 deviation (left column in both panels) and ± 0.1 deviation (right column in both two panels). In the case of the imaginary part the dashed (dotted) lines indicate a deviation of ± 0.005 ($\pm 50\%$). In the case of single-scattering albedo the dashed lines show a deviation of ± 0.05 .

EARLINET inversion algorithms

D. Müller et al.

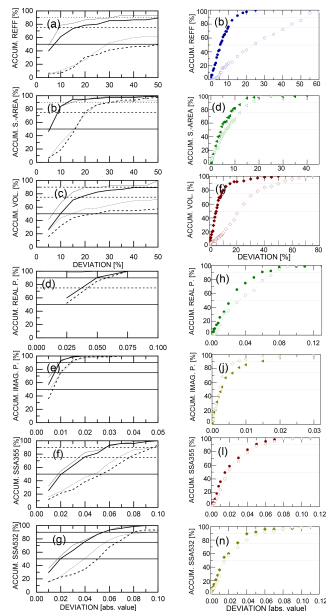


Figure 7. Accumulative distribution of inversion results for TROPOS/UH algorithm (left panel) and UH algorithm (right panel). TROPOS/UH algorithm: Results are shown for the constraint that the real part can be extracted to an accuracy of 0.05 (solid thin line) and 0.1 (solid thick line), according to Chemyakin et al. (2014) and the data error is 0 %. Results for the data error of 15 % are shown, too (0.05 accuracy as thin-dashed line and 0.1 accuracy as thick-dashed line). UP algorithm: Results are shown for the data error of 15 % (empty icons) and for the noiseless case (filled icons) without any constraint of the real part. In the case of **(a, b)** effective radius, **(c, d)** surface-area and **(e, f)** volume concentration we show the accumulative sum in dependence of the deviation in percent from the true results. In the case of the **(g, h)** real part, **(i, j)** imaginary part, and single-scattering albedo at **(k, l)** 355 nm and **(m, n)** 532 nm we show absolute deviations. The solid horizontal line shows the 50 %-level (accumulative sum). The dashed horizontal line shows the 75 %-level, and the dotted horizontal line shows the 90 %-level.

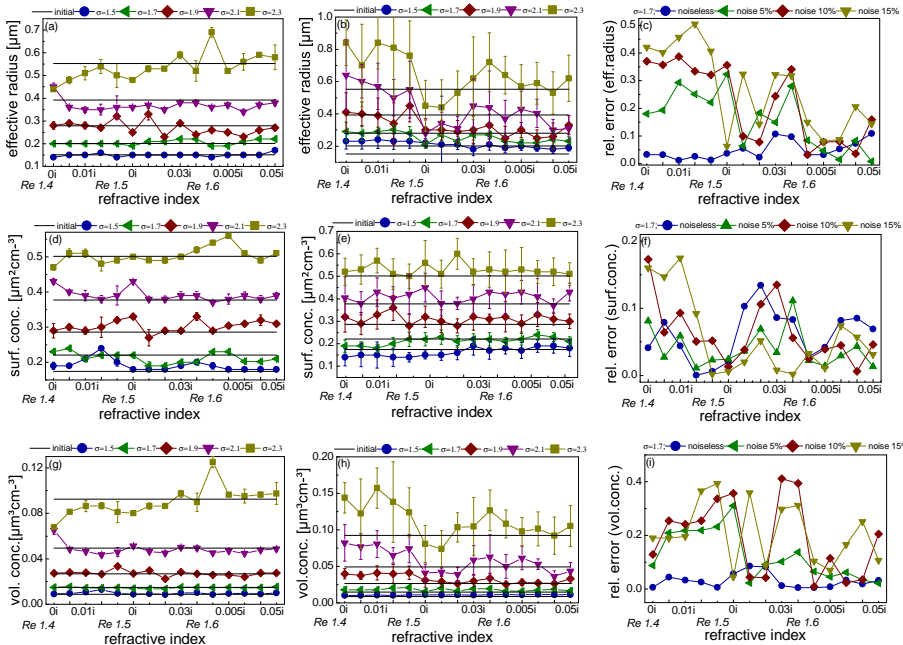


Figure 8. Retrieval results for effective radius (1st row), surface-area concentration (2nd row) and volume concentration (3rd row). First column corresponds to noiseless data. The second column corresponds to data with 15 % noise. The last column shows the relative retrieval error for increasing noise level of the input data: 0, 5, 10, 15 % for gsd 1.7 as an example. Each subfigure (**a–f**) is compartmentalized into three partition with respect to the horizontal axis (refractive index). The partitions correspond to different real parts of CRI namely 1.4, 1.5 and 1.6. Each partition shows the result for different imaginary parts of the CRI: 0, 0.005, 0.01, 0.03, 0.05/. The error bars denote the standard deviation from the mean value of all selected “best” solutions.

Title Page

Abstract

Introduction

Conclusions

References

Tables

Figures

|◀

▶|

Back

Close

Full Screen / Esc

Printer-friendly Version

Interactive Discussion



EARLINET inversion algorithms

D. Müller et al.

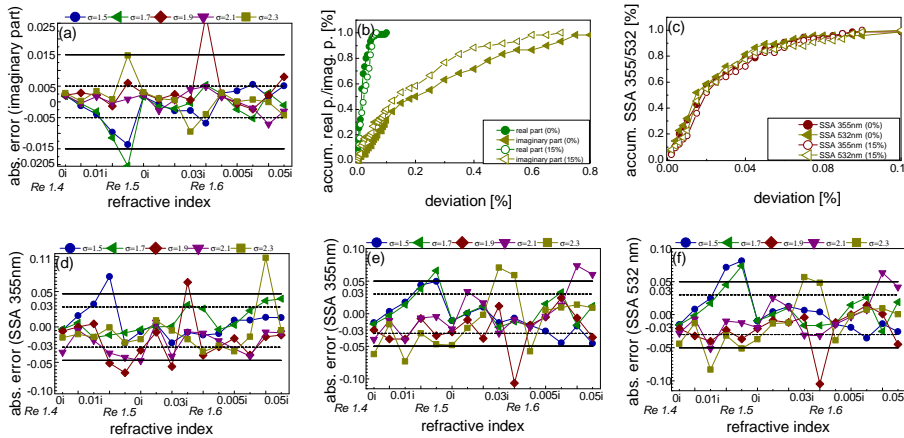


Figure 9. Relative error (deviation) development with respect to all investigated examples (accumulative distribution of inversion results): **(b)** CRI and **(c)** single scattering albedo. Absolute error of the retrieval results: **(a)** imaginary part of CRI for 15 % noisy input data, **(d–f)** SSA 355 nm (noiseless), **(e)** SSA 355 nm (15 % noisy input data) and **(f)** SSA 532 nm (15 % noisy input data). Each subfigure **(a)**, **(d–f)** is compartmentalized into three partition with respect to the horizontal axis (refractive index). The partitions correspond to different real parts of CRI namely 1.4, 1.5 and 1.6. Each partition shows the result for different imaginary parts of the CRI: 0, 0.005, 0.01, 0.03, 0.05 i .

Title Page	Abstract	Introduction
Conclusions	References	
Tables	Figures	
◀	▶	
◀	▶	
Back	Close	
Full Screen / Esc		
Printer-friendly Version		
Interactive Discussion		



EARLINET inversion algorithms

D. Müller et al.

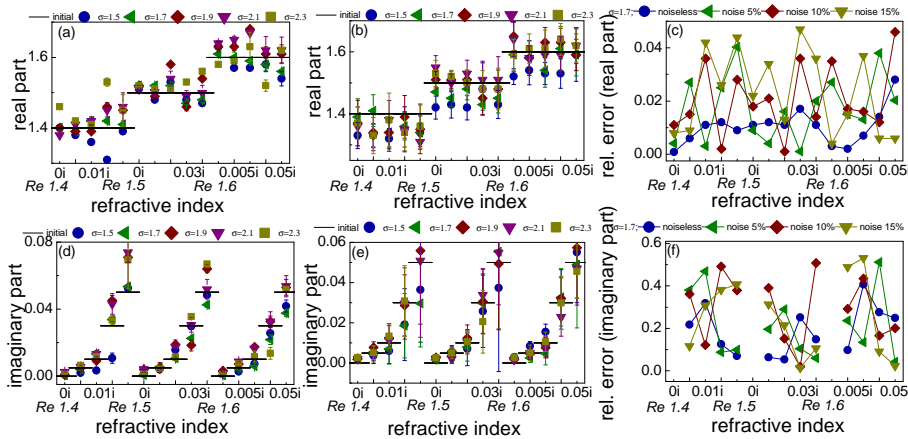


Figure 10. Retrieval results for real part of CRI (1st row) and imaginary part of CRI (2nd row). First column corresponds to noiseless and second to 15 % noisy input data. The last column shows the relative retrieval error with increasing noise level of the input data: 0, 5, 10, 15 % for gsd 1.7 as an example. Each subfigure (a–f) is compartmentalized into three partition with respect to the horizontal axis (refractive index). The partitions correspond to different real parts of CRI namely 1.4, 1.5 and 1.6. Each partition shows the result for different imaginary parts of the CRI: 0, 0.005, 0.01, 0.03, 0.05/. The error bars denote the standard deviation from the mean value of all selected “best” solutions.

Title Page

Abstract

Introduction

Conclusions

References

Tables

Figures

◀

▶

◀

▶

Back Close

Full Screen / Esc

Printer-friendly Version

Interactive Discussion



EARLINET inversion algorithms

D. Müller et al.

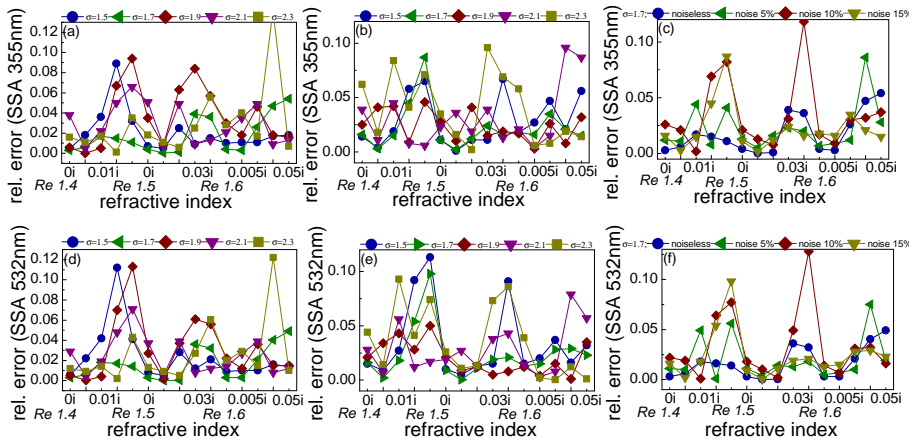


Figure 11. Relative error of the retrieval results for SSA 355 nm (1st row) and SSA 532 nm (2nd row). First column corresponds to noiseless and second to 15 % noisy input data. The last column shows the relative retrieval error with increasing noise level of the input data: 0, 5, 10, 15 % for gsd 1.7 as an example. Each subfigure (**a–f**) is compartmentalized into three partition with respect to the horizontal axis (refractive index). The partitions correspond to different real parts of CRI namely 1.4, 1.5 and 1.6. Each partition shows the result for different imaginary parts of the CRI: 0, 0.005, 0.01, 0.03, 0.05*i*.

Title Page

Abstract

Introduction

Conclusions

References

Tables

Figures

|◀

▶|

◀

▶

Back

Close

Full Screen / Esc

Printer-friendly Version

Interactive Discussion

